A 1500-years record of North Atlantic storminess from the Shetland Islands (UK)

Katharina Hess (✉ katharina.hess@geow.uni-heidelberg.de)

  Institute of Geography, Heidelberg University; Institute of Earth Sciences, Heidelberg University

Max Engel

  Institute of Geography, Heidelberg University; Royal Belgian Institute of Natural Sciences

Tasnim Patel

  Royal Belgian Institute of Natural Sciences; Department of Biology, Ghent University

Polina Vakhrameeva

  Institute of Earth Sciences, Heidelberg University

Andreas Koutsodendris

  Institute of Earth Sciences, Heidelberg University

Eckehard Klemt

  Ravensburg-Weingarten University (RWU)

Thor H. Hansteen

  GEOMAR Helmholtz Centre for Ocean Research Kiel

Philipp Kempf

  Institute of Geological Sciences, Freie Universität Berlin

Sue Dawson

  Geography and Environmental Science and UNESCO Centre for Water Law, Policy, and Science,
University of Dundee

Isa Schön

  Royal Belgian Institute of Natural Sciences; Research Group Zoology, University of Hasselt

Vanessa M. A. Heyvaert

  Royal Belgian Institute of Natural Sciences; Department of Geology, Ghent University

---

Abstract

Severe storm surges pose a major hazard to the coasts of northwestern Europe. Therefore, high-resolution records of past North Atlantic storminess are required to assess (i) whether storm activity has increased in recent decades and (ii) which future risks may arise from storm surges. This study aims to decipher storm-induced overwash processes in lacustrine sediment cores from a coastal lake on the Shetland Islands by investigating distinct sand and peat layers. This multi-proxy study utilises a range of methods such as; Bayesian AMS-^{14}C and ^{137}Cs age-depth models, cryptotephra, sedimentological, and geochemical (i.e., XRF, TOC) analyses, and the re-analysis of historical data. The XRF Si/Ti ratio and the unimodal grain-size distribution clearly show that the sand layers originate from the beach and thus are representative of storms originating from a northwesterly direction. Phases of higher storminess occurred 980−1050, 1150−1300, 1450−1550, 1820−1900 and 1950−2000 AD which correlate with a positive North Atlantic Oscillation mode enhancing water inflow into the Norwegian Sea. High-intensity storms from other directions than north(west) and a southward shift of storm tracks prevailed during the Little Ice Age (LIA, 1400−1850 AD). During warm phases of the last 1500 years, storm tracks have shifted towards the northeast Atlantic, thus confirming a possible trend for future storm track changes and increased storminess in the northern region of the North Sea as predicted by the Intergovernmental Panel on Climate Change (IPCC).

Introduction

Severe storm surges pose a major hazard to the coasts of northwestern Europe with net coastal erosion as well as detrimental effects on both infrastructure and human populations. With rising sea levels and a higher sensitivity of the global hydrological cycle as a consequence of climate change, storm-induced coastal flooding is predicted to occur in shorter time intervals in the future (Rahmstorf, 2017; Arias et al., 2021). In northwestern Europe, an increase in storminess with a poleward shift of storm tracks is expected (Goslin and Clemmensen, 2017; Seneviratne et al., 2021), whereby 'storminess' refers to both the intensity and the frequency of storms (Clarke and Rendell, 2009; Orme et al., 2015; Kylander et al., 2020). Simultaneously, global warming reduces the meridional temperature gradient of the high latitudes with the effect that turbulences along the polar front that produce the frontal cyclones decrease (Dawson et al., 2007; Sabatier et al., 2012).

To assess whether storm activity has increased in northwestern Europe in recent decades and to evaluate future risks that may arise from storm surges, high-resolution records of past North Atlantic (NA) storminess over timescales longer than the instrumental record are required (Clarke and Rendell, 2009; May et al., 2013; Goslin and Clemmensen, 2017). These records may be extended by the use of proxy data from sedimentary archives that reflect specific aspects of storminess at centennial to millennial timescales, e.g., coastal lakes (Liu, 2004; May et al., 2013).

Due to their prominent location in the northeast Atlantic, several such long-term records on past storminess have been established on the British Isles, mostly using aeolian drift sands as storm signals

or Br as sea spray signal, e.g., in coastal marshes in England (e.g., Swindles et al., 2018), in machairs (Gilbertson et al., 1999; Dawson et al., 2004 b), or in inland ombrotrophic peat bogs (Orme et al., 2015, 2016; Stewart et al., 2017; Kylander et al., 2020) of Scotland and Wales. These studies highlight changes in storminess during the Medieval Warm Period (MWP, 950–1350 AD) and the Little Ice Age (LIA, 1400–1850 AD) and correlate them with the North Atlantic Oscillation (NAO). The NAO Index reflects the difference between normalised mean winter (December to March) surface air pressures around Iceland and the Azores (Hurrell, 1995). Periods of higher storminess occurred regardless of whether warmer or transitional phases and a largely positive NAO (NAO+) mode (e.g., Dawson et al., 2002; Orme et al., 2015; Stewart et al., 2017) or a colder periods with a negative NAO (NAO−) mode prevailed (e.g., Dawson et al., 2002, 2004 b; Hansom and Hall, 2009). This association with both phases of the NAO thus provides an ambiguous picture of storm dynamics in the NA.

The Shetland Islands are located in a crucial geographic position for reconstructing palaeo-storminess since cyclones which mostly form near Iceland, pass by the Shetlands prior to reach the densely populated coasts of mainland Europe. Mainland is the largest island of the Shetlands and the only studies of palaeo-storminess from northern Mainland are based on dating cliff-top storm deposits (CTSD), which are quarried by exceptional waves and transported onshore during major storm events (Sommerville et al., 2003; Hall et al., 2008; Hansom and Hall, 2009). The timing of the deposition of these events is indirectly derived by dating the peat or sand underlying large boulders, or by lichenometry (Hall et al., 2008; Hansom and Hall, 2009). These chronologies therefore contain considerable uncertainty, hence more precise data on the variability of regional storminess are needed, helping to better understand the climatological drivers and their role in predicting future storm trends.

Since they offer precise dating and good preservation of coarser sediments as storm signals (Goslin et al., 2018), peat-dominated coastal environments, such as northern Mainland, are among the most suitable sedimentary environments to reconstruct storm dynamics. The sand in these deposits can be well-discriminated from the organic-rich background sedimentation using both sedimentological and geochemical approaches (Osleger et al., 2009). Therefore, to address the knowledge gaps described above, in this study two sediment cores (spanning c. 1500 years), from the coastal freshwater lake Loch Flugarth in the north of Mainland (Fig. 1) are investigated.

The aims of this study are to test (i) if sandy layers from the lake sediment core in the otherwise peaty sediment represent overwash and can be used to reconstruct palaeo-storminess; (ii) if phases of higher or lower storminess can be deduced from the lacustrine sediment record; and (iii) if temporal variability of past storminess can be related to variability of (supra-)regional climate patterns and drivers, e.g., the NAO, to inform future regional predictions. In addition, the Flugarth sediment core is further investigated for cryptotephra to examine whether specific historical eruptions can be used for improving and validating the age-depth model.

Study Area

The Shetland Islands represent the northernmost part of the British Isles and comprise a group of more than hundred islands (Mykura et al., 1976). Mainland accounts for 65% of the total land area (Bradwell et al., 2019).

Geology, geomorphology and soils

The Shetland Islands mostly comprise metamorphic and metasedimentary rocks of the Caledonian orogeny (Mykura et al., 1976; Gillen, 2003). Thick-banded hornblendic and granulitic gneisses dominate the catchment of Loch Flugarth together with thick lenses of amphibolite and metagabbro. At some places, impure pebbly quartzites occur (Mykura et al., 1976). The Flugarth Fault crosses Loch Flugarth from southwest to northeast (Pringle, 1970).

During the Pleistocene, the Shetlands were covered by ice (Bradwell et al., 2019; Hall et al., 2021). Radial ice-flow patterns from erratics and glacial bedforms prove the occurrence of an independent icecap on the central ridge without connection to the Fennoscandian Ice Sheet or the British Isles Ice Sheet during the Last Glacial Maximum (Bradwell et al., 2019). Postglacially, the relative sea level (RSL) rapidly rose until c. 7000–6000 a BCE and slowed down afterwards, with the last 1500 years experiencing RSL rise probably in the range of a few centimetres only (Bondevik et al., 2005; Dawson et al., 2006). Postglacial emerged beaches or raised glacial-marine sediments as indication of mid-Holocene RSL high stand are absent in the Shetlands (Kelley et al., 2018; Hall et al., 2021).

The coastline of the Shetland Islands varies greatly, ranging from cliffs of up to 300 m height to peat-floored beaches (Flinn, 1974). Beaches and dunes are rare due to low sediment availability and occur only in very sheltered locations (Hall et al., 2021), such as at the study site of Loch Flugarth and Sand Voe bay, where the dunes are mapped as calcareous dunes (Dargie, 1998). The term 'voe' refers to an over-deepened and submerged glacial valley (Mykura et al., 1976; Gillen, 2003).

Peat is the major component of Shetland's landscape today covering c. 50% of the entire archipelago (Hall et al., 2021), mostly exceeding a thickness of 100 cm (Dry and Robertson, 1982). Its development presumably began during the Windermere Interstadial from 14.7 to 12.9 ka BCE (McIlvenny et al., 2013). Surrounding Loch Flugarth are predominantly humus-iron podzols and in some areas peaty gleys and rankers (Soil Survey of Scotland, 1982).

Climate

The Shetland climate is oceanic temperate, humid, with long mild winters and short cool summers (Köppen-Geiger climate class Cfc; Beck et al., 2018). The annual mean temperature in the capital city Lerwick is 7.4°C, and ranges from 3.6°C in February to 12.4°C in July and August (period 1930–2021; Met Office, 2021). Due to the warming influence of the NA and the Shelf Edge Current to the west, the climate is warmer than in other areas of comparable latitude (Bigelow et al., 2005; Kelley et al., 2018).

Precipitation is mostly associated with the passage of Atlantic depressions, which are prominent during autumn and winter (Met Office, 2016). Autumn and winter are slightly wetter with monthly mean

precipitation of 146 mm in November compared to 53 mm in May. The annual mean precipitation is 1254 mm (Met Office, 2021).

Shetland is one of the windiest places of the British Isles with a mean annual wind speed of 14.6 kn and 58 gale days per year (Irvine, 1968; Bennett et al., 1992; Hall et al., 2021). The mean wind speed is higher during winter (Met Office, 2016) with the highest mean wind speeds recorded in January (18.2 kn) and the lowest in July (10.9 kn) (Irvine, 1968). In winter, gales occur on average every two days out of five and storms can arrive from varying directions, but mostly originate from the north, west and southwest (Birnie et al., 1993; Met Office, 2016). Atlantic depressions originating in the west reach the British Isles and generate winds from southern and southwestern directions. Subsequent to passing the British Isles, the wind direction switches to north or northwest, which typically generates the strongest gusts (Lamb, 1991; Met Office, 2016). In summer, Atlantic storms take more northerly tracks and are usually weaker (Irvine, 1968).

There are three different storm track types (Fig. 1a): (i) The fast-travelling Jutland-type cyclones with high wind speeds originating over Newfoundland and passing Jutland; (ii) the Scandinavia-type cyclones created over Greenland and Iceland crossing Scandinavia north of 60° N; and, (iii) the Skagerrak-type with tracks running between types i and ii. The Scandinavia-type cyclones have long dwell times and sometimes appear almost stationary, and therefore often coincide with high tides (Petersen and Rohde, 1991; Wöffler, 2016). For the Shetland Islands storminess is particularly driven by the Scandinavia and the Skagerrak types.

Loch Flugarth and Sand Voe bay

Loch Flugarth (60° 36' N, 1° 20' W) is a small (0.16 km²) lake located in northwestern Mainland (Fig. 1b). The lake is about 2 m asl (above mean sea-level) and separated from Sand Voe bay by a c. 70 m wide sand-and-gravel barrier (Fig. 1c). The barrier has a flat beach and is topped by a dune. Sand Voe is a relatively shallow bay opening towards the northwest and is framed by cliffs higher than 10 m (Flinn, 1974). A cemetery and a road are located between the sand beach and the lake indicating low mobility of the barrier system in recent times.

Loch Flugarth has a flat bottom and a maximum water depth of c. 2.4 m (Murray and Pullar, 1908). It is characterised by the absence of thermal stratification (Bennett et al., 1992). Non-varved polymictic lakes with a simple bathymetry such as Loch Flugarth are considered to be very suitable for recording sediment layers from flooding events because post-depositional disturbance of strata through internal processes such as hyperpycnal flows or interflows are less likely (Schillereff et al., 2014).

Loch Flugarth has a low alkalinity due to the prevailing grassland, heather and bog surrounding it (UK Centre for Ecology & Hydrology, 2004). Two small inflows from (south-)western directions are the only tributaries into the lake. There is an outflow between the beach and the lake, which is only active as a pathway for marine inflow during exceptionally high sea levels, but not active during regular high tides. During high tides the beach berm is entirely submerged by seawater and the foredunes show erosional

scarps from recent winter storms (Fig. S1). This indicates that low-frequency, high-intensity storms may create overwash and introduce seawater and sand from the beach and dunes into the lake as described, e.g., in Liu (2004) and Chaumillon et al. (2017).

Potential limitations of the study site for reconstructing storm overwash

Accurate reconstruction of past storms is based on the pre-requisite that the sedimentary archive did not change significantly. Available satellite imagery and historical maps do not show any notable changes during the last 200 years. RSL rise would increase the archive's sensitivity by shifting the shoreline inland (Sabatier et al., 2012) and lowering the threshold of overwash (Liu, 2004; Biguenet et al., 2021). However, Bondevik et al. (2005) have shown that significant RSL changes over the last 1500 years are unlikely; this is also supported by a combination of recent measurements and geological proxy data, including continuous Global Positioning System measurements, glacial isostatic adjustment models and tide gauge data from Shetland (Wahl et al., 2013).

Post-depositional erosion inside Loch Flugarth can also be excluded, as both cores FLUG 2 and 3 were taken in the central (i.e., deepest) parts. Although wind-generated waves on the lake surface may generate turbulence in the water column and promote resuspension of bottom sediment (Schillereff et al., 2014), the lake has a very small fetch and wind waves are expected to have only a minimal impact on the coring site.

Material And Methods

Fieldwork

Four short sediment cores were taken from the northern part of Loch Flugarth at a water depth of c. 2.0 m (Figs. 1d, S1) in March 2018 using a zodiac and a UWITEC gravity corer, equipped with transparent PVC liners with an inner diameter of 60 mm (Fig. S2b). Sampling localities were chosen from central (i.e., deeper) parts of the lake with sufficient distance to the shoreline to avoid disturbance by wind waves or from erosion at the subaquatic slopes. Three short sediment cores (FLUG 2–4) were taken directly from the lake bottom down to depths of up to 91.7 cm (Fig. 1d). Core FLUG 1 was taken using a Russian chamber corer mounted on a manual Edelman coring system and opened at a depth of 200 cm below the lake bottom in order to sample at a depth of 200–250 cm below the lake bottom. Additionally, two surface samples of modern sedimentary environments were taken from the shallow lake bottom close to the barrier (FLUG-M1) and from the uppermost subtidal zone of the marine embayment (FLUG-M2). In this study, we focus on sediment cores FLUG 2 and 3 with a length of 77.0 and 91.7 cm, respectively, and the two modern surface samples (FLUG-M1 and -M2).

Physical and textural sediment analysis

Sediment cores were cut and split in the laboratory of the Geological Survey of Belgium. The lithostratigraphy was described in terms of grain size, colour and organic macro-residues. In total, 91 samples from FLUG 3 were taken with an average step size of 1.0 cm. At some depths, the step size was smaller to stay within lithostratigraphic boundaries. The samples were taken in 2.0 cm steps below 79 cm below sediment surface (b.s.).

Geotek core logging and computer tomography

Core FLUG 3 was analysed using a Geotek multi-sensor core logger at the Renard Centre of Marine Geology, Ghent University, Belgium. The core logger was equipped with a Geoscan IV line scan camera for high-resolution core photographs, a γ-ray attenuation densometer to measure bulk density and a spectrophotometer (Konica Minolta CM−700d) to measure the spectrophotometric reflectance and the CIE colour spectrum (Geotek, 2021). All parameters were measured with a spatial resolution of 2.0 mm.

X-ray computer tomography (CT) scans of FLUG 2 and FLUG 3 were produced by a Siemens Somatom Definition Flash Medical X-ray CT scanner at Ghent University Hospital. The reconstructed image stacks have voxel sizes of 0.15 mm × 0.15 mm × 0.3 mm. Stacked images of the cores were analysed using the Fiji image processing package (Schindelin et al., 2012). The scanner creates a three-dimensional (3D) space to analyse the external and internal structure of the sediment core.

Grain-size analysis by laser particle diffraction

Grain-size analysis was carried out in the Laboratory for Geomorphology and Geoecology, Heidelberg University, Germany, using a Fritsch Analysette 22 NeXT Nano device with a measuring range of 0.01−3800 µm (Fritsch GmbH, 2020). The pre-treatment of samples included drying at 105°C and manual grinding to carefully break up aggregates. Organic matter was dissolved using H_2O_2 (30%). Aggregates were further dispersed using using a distilled water solution with 0.1 mol $Na_2P_2O_7$ (44.6 g l^{-1}) in an overhead shaker. The triplicate measurements of grain-size distribution (GSD) were averaged and univariate statistical measurements were calculated after Folk and Ward (1957) using GRADISTAT (v.9.1) (Blott and Pye, 2001). To statistically group entire GSDs and correlate them with facies types, end-member modelling analysis (EMMA) was applied using the R package EMMAgeo (Dietze et al., 2012; Dietze and Dietze, 2019).

Geochemical sediment analysis

Total organic and inorganic carbon

Total organic carbon (TOC) and total inorganic carbon (TIC) were analysed using an Elementar soliTOC cube in the Laboratory for Geomorphology and Geoecology, Heidelberg University, Germany. This analysis is based on dry combustion with a temperature ramp procedure and CO_2 detection with a detection limit of < 15 µg (Elementar, 2020).

X-ray fluorescence (XRF) spectroscopy

Non-destructive XRF-spectroscopy was performed using an Avaatech (GEN-4) X-ray fluorescence core scanner at the Institute of Earth Sciences, Heidelberg University, Germany. The core scanner was equipped with an OXFORD 'Neptune 5200' series 100 W X-ray source with a Rhodium anode. The slit size was adjusted to 5.0 mm downcore and 10.0 mm cross-core. Measurements were carried out at two energy levels: specifically, at 10 kV with a current of 500 µA without a filter and a dwell time of 10 s and at 30 kV beam with a 1500 µA current, a Pd-thick filter and dwell time of 10 s. Data processing was performed using bAxil software (Brightspec, 2015). To remove potential elemental bias due to topographic variations of the core surface, e.g., water content or porosity, the elements were normalised by dividing the intensity counts of each element by the XRF total during each run excluding coherent and incoherent scattering (Kern et al., 2019).

The interpretation of the geochemical analysis is based on a principal component analysis (PCA), which was carried out on 13 centered log-ratio transformed elements (Al, Br, Ca, Fe, K, Mn, Mo, P, Rb, S, Si, Sr, Zr). The hierarchical clustering of principal components (HCPC) was applied based on the first five PCs of the PCA to discriminate the most meaningful variables (i.e., elements) and to group similar sediment layers with overlapping characteristics from the variables. The PCA and the HCPC were performed in R studio following Kassambara (2017) using the R packages FactoMineR (v.2.4) for computing and factoextra (v.1.0.7) for visualisation of the results.

Chronology

A combination of ^{14}C and ^{137}Cs dating was used and integrated into a Bayesian age-depth model. The ^{14}C samples of both cores, FLUG 2 and 3, were taken at six different depths and analysed by accelerator mass spectrometry (AMS) in the Poznán Radiocarbon Laboratory, Poland (Goslar et al., 2004). Five ^{14}C dates were based on terrestrial plant fragments and one was from bulk peat, as plant macrofossils were extremely rare. All ^{14}C samples were from FLUG 3 except for one sample from FLUG 2 (Table 1). The ^{14}C data were calibrated using the IntCal20 curve (Reimer et al., 2020). A lake-reservoir effect based on older peat introduced by surface runoff or by old groundwater in similar environments (Björck and Wohlfarth, 2001) was circumvented by dating macro-plant fragments in all cases except sample FLUG 3-30-31 (Table 1).

Table 1

^{14}C data of samples from the current study.

Sample ID	Lab number	Material	Depth (cm b.s.)	δ^{13}C	^{14}C age (BP)	Error	Age in cal. a CE (2σ)
FLUG 2 ^{14}C-1	Poz-123190	Plant remains	10.5	-25.4	175	± 30	1658−1950*
FLUG 3−16 ^{14}C	Poz-127787	Plant remains	14.7	-34.0	150	± 30	1667−1950*
FLUG 3-30-31	Poz-138860	Organic-rich sediment	30.5	-32.9	1265	± 30	(666−775)
FLUG 3 ^{14}C-3	Poz-123189	Plant remains	55.5	-31.1	830	± 30	1167−1267
FLUG 3 ^{14}C-4	Poz-123187	Plant remains	63.0	-37.1	1710	± 35	(250−416)
FLUG 3−80 ^{14}C	Poz-127788	Plant remains	74.0	-49.0	1560	± 90	261−651

For ^{137}Cs dating, the upper 15 cm of one half of core FLUG 2 were sampled at 1 cm resolution. Material was freeze-dried and homogenised at the Institute of Earth Sciences and in the Laboratory for Geomorphology and Geoecology, Heidelberg University, Germany. The ^{137}Cs measurements were carried out by γ-spectrometry on a high-purity Germanium detector (Canberra BEGe5030) at the University of Applied Sciences Ravensburg-Weingarten, Germany. The ^{137}Cs activity for each sample was measured for 24 h. The detection probability was calculated using LabSocs software (Canberra). Self-absorption in the sample and in the sample cup was considered. The depths of the three ^{137}Cs peaks (1986, 1963, 1959) were calculated by a model after Smith (Aquascope) (Smith et al., 2005) (Table S1). Each peak decreases with a sum of three exponential functions each for wash-off, increasing fixation and equilibrium processes. Considering diffusion and turbation, the sum of the nine exponential functions was convolved by a Gaussian curve.

Bayesian age-depth modelling was carried out using rBacon (Blaauw and Christen, 2011). It was based on the calibrated ^{14}C and ^{137}Cs data and considered the influence of sedimentation conditions, e.g., changing sedimentation rates or events. A depth file of 0.2 cm steps was created and implemented into the model to better correlate the resulting years with the Geotek and XRF data. A thickness of 1 cm was set resulting in an age-depth model with 70 sections to obtain a model as smooth as possible with sufficiently high resolution (Blaauw and Christen, 2011).

Cryptotephra analysis

Cryptotephra analyses were conducted (i) to evaluate the presence of volcanic glass shards in the Flugarth record and, (ii) to link tephra shards to known historical volcanic eruptions based on their geochemical fingerprints.

Extraction of glass shards

Cryptotephra analysis for core FLUG 3 was performed on 5 cm-long contiguous samples, except for the lowermost sample (85–91.5 cm). Sample processing followed the procedures described in Turney (1998), Davies et al. (2005) and Blockley et al. (2005), and was previously applied to coastal peat records from European high-latitude settings (Vakhrameeva et al., 2020). First, 0.5 g of freeze-dried and homogenised sediment was immersed in HCl (10%) for 0.5 hr to remove carbonate material. The 20–100 µm grain-size fraction of the sediment was isolated by wet-sieving. Density separation of the 20–100 µm fraction into three density classes was carried out using sodium polytungstate (SPT). The 2.3–2.5 g cm^{-3} density fraction, which is expected to contain high-Si volcanic glass, was transferred into rectangular plastic lids using ethanol and dried prior to inspection for glass shards under an optical microscope. Identified shards were handpicked and mounted in transparent epoxy resin moulds with subsequent grinding and polishing of the mounts.

Electron probe microanalysis (EPMA)

Single-shard EPMA was carried out at GEOMAR, Kiel, Germany using a wavelength-dispersive electron microprobe JEOL JXA 8200. The analytical conditions included 15 kV accelerating voltage, 6 nA beam current and 5 µm beam size. To minimise Na loss during analysis, Na was analysed first. Reference samples such as basaltic glass VG-A99, rhyolitic glass VG-568 and scapolite R6600-1 (Jarosewich et al., 1980) were utilised as secondary standards and regularly measured at the beginning of each analytical session, after having analysed 40 samples and also at the end to ensure interlaboratory analytical consistency. The Lipari obsidian (Hunt and Hill, 1996; Kuehn et al., 2011) and the Old Crow tephra (Kuehn et al., 2011) were analysed as unknowns (Supplement 2). The EPMA data were normalised to 100% total oxides on a volatile-free basis. Analyses with low (< 90%) and high (> 102%) values of total oxides were excluded.

Evaluation of historical records

To attempt to correlate individual sand layers of the sediment cores with specific overwash events such as major storms, pre-instrumental data was exploited from historical documentation from Lamb (1991). Lamb (1991) describes and categorises over 166 storms for the entire North Sea region using scientific literature, local archives, diaries and newspapers since 1500 CE. The author establishes a storm severity index based on the rating of the following parameters: 'greatest wind speed', 'greatest area covered at any stage by winds causing widespread damage' and 'total duration of the occurrence of damaging winds'. The storm severity index ranges from Class VI (low severity) to Class I (very high severity). Four conditions were established to consider a historical storm to be relevant for the sedimentary archive of Loch Flugarth:

1. minimum Class V,
2. minimum Beaufort Scale 10 (if available),
3. geographical description with tags: 'Shetland', 'Northern North Sea', 'Northern Scotland', 'Northern part of the British Isles' or 'Eastern North Atlantic' and
4. western to northern wind direction, due to the exposure of Sand Voe's entrance.

All considered storms were chronologically compiled in an Excel file with all relevant information such as date, time span, duration, wind direction and speed, severity (after Lamb, 1991), location, description and reference. All dates were expressed in the Gregorian calendar and historical dates before October 1582 CE were stated in the new style.

Results

Chronostratigraphy

Age-depth modelling reveals a chronostratigraphy of about 1500 years, dating back to 426–787 cal. a CE. The averaged accumulation rate across the entire core was 20 a cm^{-1}, whereas the uppermost 15 cm dated by ^{137}Cs revealed 10 a cm^{-1} (Fig. S3). Further details on the results of age model construction can be found in Supplementary Note 1.

Lithostratigraphy

Cores FLUG 2 and 3 showed lacustrine sediments being visually separated into four different facies. Both cores were taken c. 20 m apart. Their stratigraphic correlation was excellent (Fig. 2). All lithostratigraphic descriptions refer to depths identified in FLUG 3. Facies 1 comprised muddy, organic-rich, dark brown sediment. At 37.5–43.0 cm b.s. and 73.0–77.0 cm b.s., respectively, these organic-rich deposits were much brighter in colour and defined as Facies 2. Facies 3 comprised muddy, organic material mixed with sand grains, dominant in the lower part of the core at 57.0–73.0 cm b.s. Facies 4 was represented by bright sand layers of varying thickness from a few millimetres up to several centimetres. At the base of the core, Facies 4 was c. 13.0 cm thick. These basal sands did not represent the bottom of the lacustrine sequence as in FLUG 1 (200–250 cm b.s.) dark, organic-rich background deposits of Facies 1 still continued (Fig. S3).

A total of 42 bright sand layers (facies 4) were identified mainly based on the CT scans. The most pronounced Facies 4 deposits were found at c. 3.0–8.5 cm (L1–5), 14.2–14.8 cm b.s. (L11), 16.0–17.4 cm (L12), 26.8–27.1 cm (L17), 32.7–33.0 cm (L18), 35.0–35.7 cm (L19), 36.0–36.5 cm (L20), 50.0–56.0 cm (L27–35) and 78.0–91.7 cm (L41–42). Sharp basal boundaries of sand occurred at 5.0, 7.0 and 78.5 cm in FLUG 3.

According to the lithostratigraphy, FLUG 3 can be divided into seven different units: Unit I 0–18 cm b.s. revealed 12 visible sand layers (Facies 4). A rounded fine pebble (> 0.5 cm) occurred at the bottom of Unit I. Furthermore, two pieces of wood were identified: one of 4.0 cm length at 11.0–12.0 cm b.s. in FLUG 2

(Fig. 2a) and another one of 3.5 cm length at 12.0–13.5 cm b.s. in FLUG 3 (Fig. 2b). Unit II (18.0–35.0 cm) contained the darkest sediments of the entire core (Facies 1). Distinct sand layers were rare. A flat, subangular, grey pebble was found at a depth of 30.5 cm b.s., resembling pebbles from the modern beach (FLUG-M2). All pebbles in the core were found at upper or lower contacts of sand layers. Unit III (35.0–39.0 cm) was characterised by three very distinct sand layers (L19–21) with a thickness of up to 1.5 cm each. Similar to Unit I, these layers were more dominant than background Facies 1. From Unit III to Unit IV (39.0–49.0 cm) there was an abrupt change from Facies 1 to Facies 2, with Facies 1 and Facies 3 reappearing again in the lowermost part. Unit V (49.0–57.0 cm) contained seven distinct sand layers with clear horizontal boundaries, each of them ≥ 0.5 cm thick. Unit VI showed a background of mainly Facies 3, with a short section of Facies 1 in the uppermost part. Ten distinct but thin sand layers were counted with thicknesses of only a few millimetres. Unit VII differed from the rest of the core as it comprised one thick compound sand layer (L41, L42).

The density data of FLUG 3 (Fig. 3) reflected facies changes well, with the lowest densities (< 1.0 g cm^{-3}) found in the upper 3 cm and the highest densities in the lighter sandy layers (peak densities of about 2.0 g cm^{-3}). The CIE colour space data reflected similar trends, such as *b axis (yellow colour space, proxy for light sand). Most measurements ranged between − 1.0 and + 2.5. Only at depths with purest sand layers, such as 35.9–36.3 cm b.s., 75.9–76.5 cm b.s. and in particular 81.7–91.7 cm b.s. values were > 3.0.

Sedimentological characteristics

The grain-size analysis included particles from 0.01 µm (clay) to 700 µm (coarse sand) (Fig. 3). The GSD ranged from unimodal and well-sorted to trimodal and very poorly-sorted. Sand content > 90% was detected at depths of 4.0–5.0 cm b.s. (L3), 7.0–8.0 cm b.s. (L5), 16.0–18.0 cm b.s. (L12), 54.5–55.0 cm b.s. (L31) and 56.0–56. cm b.s. (L32). In general, Facies 4 had a unimodal, poorly to moderately well-sorted GSD; it was better sorted than Facies 1. Modern samples from the lake margin close to the sandy barrier (FLUG-M1) and the uppermost subtidal zone (FLUG-M2) had very similar grain-size characteristics (Fig. S5). Both GSDs were unimodal and moderately well-sorted fine sand with sand content of > 96% and a mean value of 218 µm.

End-member modelling of GSDs revealed three distinct end members (EMs) (Fig. 4). EM 1 depicted a unimodal, moderately well-sorted symmetrical curve with a mode in fine sand. It is best represented by samples from the most prominent intercalated sand layers, such as 4.0–5.0 cm b.s. (L3), 7.0–8.0 cm b.s. (L5), 35.0–36.0 cm b.s. (L19), 38.0–38.5 cm b.s. (L21) and 54.5–55.0 cm b.s. (L31). EM 2 was characterised by a bimodal, poorly-sorted curve, categorised as muddy sand. It was similar to some of the samples from the basal sand unit, but seemed to represent a mixture between different sources and processes. EM 3 was a very poorly-sorted, trimodal curve with peaks at about 5 µm, 20 µm and 200 µm, categorised as a fine sandy coarse silt. It had a large overlap with Facies 1–3, in particular samples from 34.0–35.0 cm b.s. and 57.5–58.5 cm b.s. Both surface samples from the seaward barrier and the uppermost subtidal zone resembled EM 1 (Fig. 4).

Geochemical proxies

The PCA was first conducted on the XRF elements with the first two PCs explaining 47.2% (PC1) and 14.0% (PC2) of the variance of the whole dataset (Fig. S6), respectively. PC1 was dominated by the variance of Al, Br, K, Rb, S, Si and Zr, and PC2 was dominated by Ti.

XRF results are typically presented in ratios with conservative elements (e.g., Ti, Fe, Si) as denominator. The ratios were selected based on the results of the PCA of the elements (Fig. S6). Ti was used in particular, as it is not involved in biogenic processes and is neither affected by redox conditions nor by diagenetic overprinting (Chagué, 2020). Figure 5a shows the variables together with 50 selected samples. Based on the eigenvalues, five dimensions and four clusters were collectively considered for the HCPC. In the HCPC (Fig. 5b), Facies 4 was geochemically divided into the basal sands (blue cluster 1), represented by Zr/K and Sr/Br, and upper thin sand layers (grey cluster 3), mostly driven by Si/Ti and K/Ti. The remaining darker Facies 1 sediments were separated into a pure, fine-grained, organic-rich group (red cluster 4) e.g., at 20.0–30.0 cm b.s., with high concentrations of Ca, S, Br and Mn, and a mixed group (yellow cluster 2), mostly comprising samples from Facies 2 and 3 (Fig. 5).

The most representative ratios for each cluster were Sr/Br (cluster 1), Si/Ti (cluster 3), and S/Ti (cluster 4) (Fig. 6). The TOC content of FLUG 3 varied between nearly 0% at the bottom of the core and up to > 35.0% at a depth of 29.0 cm (Fig. 6). The measured TOC was higher in Facies 1 layers with an average of about 20.0%. The lowest values occurred in homogenous sand layers e.g., in L41–42. TOC of FLUG-M1 and FLUG-M2 was nearly 0%, too. TIC values were close to 0% in the entire core.

Cryptotephra record

Of the 18 samples processed and examined for cryptotephra, all but the two lowermost samples from the basal sand (Unit VII) yielded tephra shards. The shard counts ranged from 6 to 194 shards per 0.5 g of dry weight sediment (gdw). The concentration profile of the glass-shards showed three peaks at 25.0–30.0 cm, 40.0–45.0 cm and 55.0–60.0 cm core depth (Fig. 7), respectively.

The glass compositions were mostly classified as rhyolites and dacites and only a few shards fell into the basaltic and trachydacitic fields (Fig. 8a). In total 10 glass geochemical populations (P1 to P10) were identified in FLUG 3. Besides major-element bivariate plots, a PCA of the EPMA data was used to facilitate discrimination between silicic glass populations (Fig. 8c). PC1 and PC2 explained 68.0% and 13.0% of the total variance in the dataset, respectively. PC1 was characterised by positive loadings of TiO_2, Al_2O_3, FeO, MgO, CaO, and Na_2O and negative loading of SiO_2, K_2O, and Cl. PC2 was dominated by positive loadings of Na_2O and Cl and negative loadings of MgO, K_2O, and TiO_2.

Most of the geochemical populations occurred in multiple samples throughout the core, with two to six populations being present in each sample (Table S3; Fig. 7). All glass populations could be assigned to various Icelandic volcanic centres including Vatnajökull (P10), Öræfajökull (P9), Torfajökull (P8), Katla (P7 and P1), Hekla (P46), Askja (P3) and Veidivötn-Bárdarbunga (P2) (Figs. 7, S8–S13). A description of

each glass population can be found in Supplementary Note 2. Full EPMA glass data can be found in Supplement 2.

The historical record

The evaluation of storminess from historical data revealed that a total of 77 storms affected northern Scotland and the northern North Sea originating from a western to northern direction (Lamb, 1991). Based on the total number of storms, a high storm frequency was recorded in the second half of the 20th century, particularly during the 1980s, and in the 19th century, with seven and eight severe storms during the 1880s and the 1820s, respectively (Fig. 9). For the first half of the 20th and the 18th century, a comparably low number of storms was documented. In contrast, the 1690s–1710s were known for their intense storminess with recurring sandstorms along the Scottish coasts (Lamb, 1991; Bampton et al., 2017). A longer period of high storm frequency can be observed between the 1540s and 1610s with a calmer phase in the 1560s (Lamb, 1991).

Most of the storms occurred in winter (Dec, Jan, Feb), particularly those of the 20th century (Fig. 10). The 19th century was characterised by several heavy summer storms (Jul, Aug, Sep) and severe winter flooding due to higher rainfall. Most notable is the high number of storms in spring (Mar, Apr, May) during the 18th century. During the 16th and 17th century, storminess was high during late summer and autumn (Aug–Nov). Thus, there is an apparent shift from spring and autumn storms during the 16th – 19th centuries towards a dominance of winter storms in recent times (20th century) (Lamb, 1991).

Discussion

Sedimentary facies interpretation

The EMMA revealed tri- to bimodal GSD curves for EM3 reflecting Facies 1. Despite thorough continuous H_2O_2 treatment over several days, small amounts of organic matter may have remained in the sediment, explaining the third mode in the fine silt category at about 4 μm. The high organic-matter content originated either from autochthonous algal productivity or terrestrial run-off from peaty soils of the lakeshore (Biguenet et al., 2021). The latter may indicate heavier precipitation and/or greater snow melting (McIlvenny et al., 2013).

Facies 1 was rich in Br, Ca and S. Although Br was used as marine indicator in other studies from Scotland (Orme et al., 2015; Stewart et al., 2017), Br, Ca and S are very mobile in the sediment (Cuven, 2013; Kylander et al., 2020), better preserved in fine-grained organic matter (Chagué, 2020; Biguenet et al., 2021), and thus indicate organic-rich, peaty layers in the current study.

Since Ca is often associated with carbonates, it could either indicate biogenic production in the lake (Davies et al., 2015) or originated from marine shell fragments introduced from the beach and shallow subtidal (Kelley et al., 2018). However, neither shell remains nor any other carbonates were found in the modern intertidal environment (samples FLUG-M1 and FLUG-M2), nor do carbonates form in an acidic,

peaty environment such as Loch Flugarth. Kylander et al. (2020) found high Ca concentrations in peat-bog samples in southern Scotland and related them to the underlying metagabbro that also occurs around Loch Flugarth (Mykura et al., 1976). The calcareous fixed dune on top of the sand-and-gravel barrier (Dargie, 1998) could be another source for Ca introduced by wind or surface runoff during heavy precipitation.

Facies 2 was very silty whereas Facies 3 was poorly-sorted and had no clear elemental signal, likely representing a mixture of different sediment types. Both Facies 2 and 3 could be assigned to the mixed cluster 2 in the HCPC. In contrast to Facies 1–3, Facies 4 was better sorted and showed a unimodal GSD, best explained by EM1 in the EMMA peaking in the sand category. Additionally, EM1 was nearly identical to the GSD type for the modern samples FLUG-M1 and FLUG-M2, pointing to an unequivocal sand source at the beach and the shallowest part of Sand Voe bay. The lowermost sand layers L41 and L42 deviated from EM1; their GSD is explained to a larger percentage by EM2. This discrepancy and the formation of L41 and L42 are discussed in detail elsewhere.

Facies 4 was represented by cluster 3 in the HCPC, dominated by the ratios Si/Ti and K/Ti. In Facies 4, K and Si were the principal elements in quartz and K-feldspars, which are typically found in beach sand (Pouzet and Maanan, 2020). These ratios were used to differentiate between coastal beaches and river sand populations (Goslin et al., 2018) and as storminess indicators in peat bogs (Kylander et al., 2020). The overall high Fe content in all sediments of the core could be attributed to the humus-iron podzols surrounding Loch Flugarth (Soil Survey of Scotland, 1982).

Both aeolian transport and marine overwash may be responsible for the deposition of thin sand layers in the lake since both processes generate well-sorted GSD curves (Dawson et al., 2004 b; Morton et al., 2007; Moskalewicz et al., 2020). In a study on coastal sand movements in the Scottish Outer Hebrides, well-sorted sediments with unimodal curves and a mean grain-size of about 200 μm, very similar to Facies 4, were linked to aeolian processes, because marine indicators such as shells or other marine microfossils were absent (Dawson et al., 2004 b). However, the sharp, possibly erosional lower contact of some sand layers (Moskalewicz et al., 2020), e.g., L3, L5, or L12, and the pebbles and wood fragments directly found above or below a sand layer are typical features of storm overwash. In addition, there is no large sand supply around Loch Flugarth, which makes wind-blown sand transport unlikely. NA cyclones are associated with high rainfall. The sand around the beach becomes too wet to be transported (Arens, 1996; McIlvenny et al., 2013) which also speaks for overwash.

Tephrochronological potential of the site

Multiple cryptotephra occurences identified at Loch Flugarth were tentatively correlated with specific Icelandic eruptions based on their major-element geochemistry and age estimates according to the age-depth model of the FLUG 3 record. These included Askja eruption BTD-48 (c. 870s CE; Pilcher et al., 2005), Veidivötn-Bárdarbunga eruption SV-L1 (c. 1100s CE; Watson et al., 2016), silicic Katla eruptions GB4-50 (c. 1250 CE; Hall and Pilcher, 2002) and BTD-15 (c. 1650–1750 CE; Pilcher et al., 2005) and possibly basaltic Katla eruptions in c. 1357 CE (Larsen et al., 2014) and 1755 CE (Thorarinsson, 1981), Torfajökull

eruption GB4-45b (c. 1300 CE; Plunkett and Pilcher, 2018), and Öræfajökull eruption in 1362 CE (Ö-1362; Larsen et al., 1999) (see detailed discussion in Supplementary Note 2). Higher-resolution cryptotephra analysis (e.g., in 1-cm increments) would allow refinement of these correlations, but the FLUG 3 record already provided new evidence for the occurrence of several more tephra isochrons on Shetland, where so far only three early to middle Holocene Icelandic eruptions had been identified, i.e., Saksunarvatn Ash, Hekla 4 (H4) and Hekla-Selsund (HS) (Bennett et al., 1992; Dugmore et al., 1995; Swindles et al., 2013). In contrast, our study demonstrated the potential to extend the current tephrostratigraphy of Shetland to the late Holocene and specifically to the past 1500 years, which is essential for independent testing and refinement of site chronologies spanning this time interval. Many of the tephra isochrons identified at Loch Flugarth, most notably Ö-1362, have so far not been known from Scotland.

It is noteworthy that although the extraction of basaltic glass shards from core FLUG 3 was not conducted in this study, a few basaltic shards were detected alongside silicic glasses at three different depths (populations P1 and P2; Fig. 7). This suggests that Loch Flugarth sediments likely preserved abundant basaltic cryptotephra layers and once again highlights the importance of a targeted search for basaltic glass shards (e.g., by examining the > 2.5 g cm^{-3} density fraction) for generating complete tephrostratigraphies for northern Europe (e.g., Vakhrameeva et al., 2020).

In addition to primary cryptotephra layers, a considerable number of secondary glass shards were identified in core FLUG 3 (Supplementary Note 2). These included (i) material that was vertically displaced, both up- and down-core, from primary cryptotephra deposits occurring in the FLUG 3 core, e.g., Ö-1362, and (ii) material that represented eruptions older than the studied record (c. 590 CE) such as Hekla eruptions H4 (c. 2400−2280 BCE; Pilcher et al., 1995) and HS (c. 1800−1750 BCE; Wastegård et al., 2008), the Microlite tephra from an undefined source beneath the Vatnajökull ice cap in Iceland (c. 700 BCE; Plunkett et al., 2004), and the Glen Garry tephra from Askja (c. 230 BCE; Barber et al., 2008).

HS and H4 were previously reported from the Shetland Islands as cryptotephra layers (Bennett et al., 1992; Dugmore et al., 1995; Swindles et al., 2013), whereas Glen Garry and Microlite tephras were traced to northern Scotland (e.g., Langdon and Barber, 2001). Thus, their occurrence in the lower part of the sedimentary sequence of Loch Flugarth and/or on its catchment is very likely. Considering the substantial time gaps between the ages of these tephra isochrons and their re-deposited correlatives from core FLUG 3, it is more plausible that the tephra re-deposition was due to erosion and remobilisation of tephra shards from terrestrial sediments and soils around the lake margins and/or from the beach and dunes due to storm overwash. Re-distribution of primary tephra material in peatlands and lake sediments, both natural and through human activities, is a commonly encountered problem in tephrochronology, which was previously reported from Shetland (Swindles et al., 2013, and references therein). Our results illustrated the importance of identifying the primary fallout deposits in sedimentary sequences.

Phases of higher storminess in Shetland

The presence of Facies 4 in combination with the age-depth model indicated five phases of higher storminess: approx. 980−1050, 1150−1300, 1450−1550, 1820−1900, and 1950−2000 cal. a CE.

Increased storminess could be associated with the late 12th century and the 13th century, which belong to the MWP (L26−36), the onset of the LIA (L18−21), the Dalton Minimum ending around 1830−1840, and the 20th century (L1−L14). The period of lower storminess around 1910−1950 (c. 8−11 cm b.s.) was consistent with pre-existing regional geological (Hansom and Hall, 2009) and historical (Lamb, 1991) data.

A higher storminess from 1100 to 1300 cal. a CE could be corroborated by a proxy record from northern Scotland with a strong presence of sand layers within background peat for the MWP, which was interpreted as a wetter and stormier period (Stewart et al., 2017). Our findings are also in line with data from northwest France, where high storminess was dated to 1050−1085 and 1250−1350 cal. a CE (Pouzet and Maanan, 2020). Orme et al. (2016) provided evidence for higher storminess in two ombrotrophic peat bogs on the Outer Hebrides dated to approx. 1150 and 1550 cal. a CE, which might correlate with L30−33 and L18−21 in the Flugarth record, respectively. The 14th, 17th, and 18th centuries were predominantly calmer periods reflected by fewer and thinner sand layers. The conspicuous sediment facies change at c. 40 cm b.s. coincides with the period 1400−1420 cal. a CE, which has been described as a strong NA climate change by Dawson et al. (2007).

Several studies attributed individual sand layers to specific historical storm events during the last 300 years (Sabatier et al., 2008; Moskalewicz et al., 2020; Biguenet et al., 2021). The correlation with historical data, however, is challenging due to the high number of severe storms around the Shetland Islands. For instance, more than 21 severe storms occurred between 1950 and 1990 (Lamb, 1991), but only seven sand layers were identified in the sediment core for the same period. This discrepancy is quite common as only the most intense storms tend to be preserved in sediment records (e.g., Liu, 2004; Dezileau et al., 2011; May et al., 2013; Moskalewicz et al., 2020). Furthermore, two storms of identical intensity and characteristics may not necessarily cause the same marine flooding and sediment pattern. Changing boundary conditions such as tides, fetch, season etc. additionally influence the occurrence of overwash (Liu, 2004; Liu and Fearn, 2000; Moskalewicz et al., 2020). Any estimation of the number of storm events from individual sand layers should therefore be treated with caution (Biguenet et al., 2021). Nevertheless, the high abundance of sand layers within the Flugarth records implied a high temporal resolution especially when compared to other studies (Sabatier et al., 2008; Pouzet and Maanan, 2020; Biguenet et al., 2021).

Layer L1 most probably corresponds to a storm in the late 1980s or 1990s, possibly the severe storms in 1992 or 1993, where boulders at Eshaness at the northwest coast of Mainland close to the study site were shifted on top of the > 40 m-high cliffs by waves (Hall et al., 2006; Hansom and Hall, 2009). Layer L2 might represent the severe storm of December 1986, while L3 could either be correlated with a storm in 1983 or 1981 as the ^{137}Cs peak of 1986 lay in between these layers. The historical North Sea storm in 1953, that caused a 0.5−3.0 cm thick sandy layer in coastal peats in eastern England (Swindles et al., 2018), was also described as severe for the Shetland Islands and is likely represented by one of the sand layers L5−7.

The pronounced sand layers L11−12 might reflect the severe storms in the middle of the 19th century, e.g., the storms in 1839 or 1855 (Lamb, 1991). The relatively thick layer L12 at 16 cm b.s. dated to 1735−1901 (median: 1831) cal. a CE might have been caused by a massive storm reconstructed in North Scotland (McIlvenny et al., 2013). Although large sand movements with accumulation of several decimetres were reported in the 1690s in Scotland and the southernmost part of Shetland e.g., the Udal storm or the Culbin Sands Disaster (Lamb, 1991; Orme et al., 2016; Bampton et al., 2017), no large sand layer was found in all FLUG sediment cores during this period. Only the sand layers L16 and L17 dated to about 1706 and 1650 (1531−1745) cal. a CE, respectively, might coincide with this period. The high sand accumulation of L19−21 of 1367−1614 (median: 1506) cal. a CE might be linked to large sand movements in the Shetlands dated to 1492 and 1500 by Sommerville et al. (2003).

Atmospheric and oceanic drivers of storminess

Periods of higher storminess in the Loch Flugarth sediment core occurred during the MWP until c. 1300 and 1450−1550 and since the second half of the 19th century with a lower storminess during the first half of the 20th century (Fig. 11h−i). The NA water inflow based on coccolith populations was considered to have a major climatic impact on the Loch Flugarth study area due to the proximity of the Shelf Edge Current to the northwest coast of Shetland. The increased warm water inflow from the tropics correlated with higher storminess in Shetland, particularly in the last 150 years (Giraudeau et al., 2010) (Fig. 11d). Moreover, phases of higher storminess in the Flugarth record also corresponded to a prevailing positive NAO (NAO+) mode (Fig. 11a,h,i), although the phase of high storminess during the MWP in the Flugarth record was shorter than the NAO + phase presented by Trouet et al. (2009).

A proxy of annually laminated stalagmites from a Scottish cave based on lamina counting and U-Th dating (Fig. 11c) reflected the transition from the warm MWP into the colder LIA around 1400 and supported the persistent NAO + mode during the MWP and the NAO− mode with several smaller positive excursions during the LIA (Baker et al., 2015). The NAO− mode during the LIA could be explained by high-pressure systems that formed over the northeast Atlantic due to colder surface waters weakening the Icelandic deep pressure system. This was attributed to stationary high-pressure systems which would hinder the development of cyclones in the NA and thus reduce storminess during winter (Orme et al., 2016). However, this finding is in disagreement with the GISP2 ice core record from Greenland, where storminess was inferred from Na^+ concentrations introduced by long-distance sea spray (Meeker and Mayewski, 2002) (Fig. 11b). The GISP2 ice core record clearly indicated a higher (lower) storminess during the LIA (MWP). Other regional studies from Scotland and the Shetland Islands also showed higher storminess consistent with the GISP2 ice core particularly during the coldest phase, i.e., the Maunder Minimum (1645−1715) (e.g., Dawson et al., 2004 a, b, 2007; Hansom and Hall, 2009).

This discrepancy in records may be resolved by considering seasonality patterns (Trouet et al., 2012). Since the NAO is driven by winter weather patterns, the higher storminess during NAO− mode (i.e., LIA) may be explained by severe cyclones predominantly occurring in spring and autumn (Lamb, 1991; Trouet et al., 2012). Additional evidence for this hypothesis is provided by Wheeler et al. (2010), who inferred

severe storms during spring and autumn between 1685 and 1699 from Royal Navy logbooks. This is in line with the increased storminess observed in the historical evaluation of storminess per century in spring and autumn during the 17th to 19th century (Lamb, 1991). However, this seasonal shift does not explain why these storms were not recorded in the Loch Flugarth record.

One hypothesis could be the southward extension of the Arctic sea ice during the LIA (Dawson et al., 2002, 2010). This extension may have cooled the air and the sea surface in the northeast Atlantic. Consequently, the storm tracks were shifted further south (Dawson et al., 2002, 2010; Giraudeau et al., 2010; Orme et al., 2015; Stewart et al., 2017). Biguenet et al. (2021) emphasised that only storm tracks which ran very close on the seaward side of the coast could be captured in the sedimentary archive of a small coastal lake. Thus, even a slight shifting of the storm tracks could determine whether or not a storm was preserved in the lake record. Since the site only recorded storms with tracks north of 60°N, Jutland-type cyclones moving from southwest to northeast were therefore unlikely to be captured by the Flugarth record (Fig. 1a). The hypothesis of a larger-scale southward shift of storm tracks is supported by comparisons of studies in the Mediterranean, which found a clear link between cold phases of the Holocene (e.g., around 1550–1990) and higher storminess, whereas storminess was low during the MWP (Sabatier et al., 2008, 2012; Costas et al., 2012).

Due to its northern opening, Sand Voe bay captured storms from northerly or northwesterly directions. Based on model simulations, Bampton et al. (2017) stated that present wind fields are similar to the wind conditions of storms observed during the LIA. However, historical documents indicated more easterly and northeasterly winds during the LIA (Lamb, 1991), which would likely produce less overwash at Flugarth. In addition, the lake sediment layers with high Ca content were dated to the LIA. Northeasterly winds during the LIA could have transported Ca from the calcareous dune immediately northeast of Loch Flugarth (Dargie, 1998), which under a colder and drier climatic regime (Stewart et al., 2017) might have been less vegetated, into the lake. The high peat content in the sediment core during the late LIA was possibly introduced by increased surface discharge associated with precipitation maxima in summer or by shoreline soil erosion during the 18th and 19th centuries (Dawson et al., 2004 a).

The regional CTSD studies (Fig. 11e) showed a continuously high storminess during the LIA (Gilbertson et al., 1999; Hansom and Hall, 2009). CTSDs were found at 15–60 m asl in Shetland, and dated to 700–1050, 1300–1900, and post-1950 cal. a CE, supporting the Na^+ proxy of GISP2 (Hansom and Hall, 2009). Due to the proximity of the CTSD site to Loch Flugarth and a similar orientation of the cliffs, the high storminess between 1300 and 1900 should be also visible in the Flugarth record. However, Hansom and Hall (2009) acknowledged that the dating precision of the CTSD is relatively low due to indirect dating of adjacent sand or peat underneath the boulders. Thus, the CTSD record during the LIA might also relate to a low number of high-intensity events instead of a generally higher storm frequency (Trouet et al., 2012; Orme et al., 2016; Stewart et al., 2017). The higher intensity might be explained by the generally steepened thermal gradient between the cold polar waters and the warm subtropics during colder periods (Dawson et al., 2007; Sabatier et al., 2012). Thus, it could be inferred that the storm frequency was

relatively low during the LIA (Orme et al., 2016), resulting in a lower number of events coinciding with high tides and a lower probability of overwash at Flugarth.

Further arguments for a moderate storminess during the LIA are that aeolian sand drift does not only depend on wind strength, but also on sand availability, vegetation cover, anthropogenic impact, and drier conditions (Bampton et al., 2017). The coldest stages of the LIA were associated with a reduced winter storm frequency over the NA due to the expansion of the polar anticyclone, providing a NAO− mode and stable conditions during winter (Dawson et al., 2004 b). These high-pressure systems could have created drier conditions during the LIA (Stewart et al., 2017) and, hence, reduced vegetation cover. Together with anthropogenic landscape changes, i.e., overgrazing, sand dunes might have been less stable (Bampton et al., 2017). The recent decline in aeolian sand transport observed in Scotland over the past 200 years could be attributed to anthropogenic adaptation activities on dune systems (Orme et al., 2016).

Conclusions

This study showed that the two lake sediment cores from Loch Flugarth in the northwestern part of Mainland, Shetland Islands, recorded NA storminess over the last c. 1500 years. This multi-faceted approach using sedimentological, geochemical, chronological and historical data revealed 42 sand layers originating from the beach and the very shallow subtidal zone. The marine origin of the sand layers was concluded from the GSD characteristics and the XRF-based Si/Ti and K/Ti element ratios discriminating these sand layers from the other sediment types.

The data clearly showed phases of higher storminess around 980–1050, 1150–1300, 1450–1550, 1820–1900 and 1950–2000 cal. a CE. However, a clear correlation of individual sediment layers to single historical storm events was difficult due to the high number of historically documented storms.

Phases of higher storminess correlated with NAO + phases and enhanced NA water inflow into the Norwegian Sea. The number and thickness of storm layers dated to the MWP, particularly 980–1050 and 1150–1300 cal. a CE, as well as during the second half of the 20th century, suggested similar storm conditions. The lake sediments reflected storm tracks running north of the Shetland Islands and storms originating from northwesterly to northerly direction. Additionally, a shift of storm tracks towards the northeast Atlantic during warmer periods could be inferred.

The LIA was dominated by a different wind regime characterised by more northeasterly to southwesterly storms. In addition, storm tracks shifted further south, resulting in higher storminess in southern parts of Europe. Storminess shifted both spatially and temporally with more storms in spring and autumn rather than in winter. Winters probably were drier during the LIA due to anticyclonic weather patterns over the NA.

The higher number and thickness of sand layers in the Flugarth record in recent times confirmed that storm tracks shifted further north, as shown in the most recent IPCC report (Seneviratne et al., 2021). The combination of warmer oceans and cold fresh air from north is expected to form intense low-pressure

systems in the future, leading to more severe storms from northwest to southeast and thus higher storm surges in the wider study area (e.g., Goslin and Clemmensen, 2017).

Declarations

Conflict of interest

The authors declare no conflict of interest.

Data availability

Data reported here are stored at https://doi.org/10.11588/data/QJEZHT and freely accessible under a Creative Commons Attribution 4.0 International License (CC BY 4.0). Further supplementary data and information are available as Supplymentary Material and Supplementary Data in the online version of the paper. Correspondence and requests for materials should be addressed to K.H.

References

1. Arens, S.M., 1996. Rates of aeolian transport on a beach in a temperate humid climate. Geomorphology 17, 3–18. https://doi.org/10.1016/0169-555X(95)00089-N
2. Arias, P.A., N. Bellouin, E. Coppola, et al. 2021. Technical Summary. In: Masson-Delmotte, V., Zhai, P., Pirani, A. et al. (eds.), Climate Change 2021: The Physical Science Basis. Contribution of Working Group I to the Sixth Assessment Report of the Intergovernmental Panel on Climate Change. Cambridge University Press, Cambridge and New York, pp. 33–144. https://doi.org/10.1017/9781009157896.002
3. Baker, A., Hellstrom, J.C., Kelly, B.F.J., et al. 2015. A composite annual-resolution stalagmite record of North Atlantic climate over the last three millennia. Scientific Reports 5, 10307. https://doi.org/10.1038/srep10307
4. Bampton, M., Kelley, A., Kelley, J., et al. 2017. Little Ice Age catastrophic storms and the destruction of a Shetland Island community. Journal of Archaeological Science 87, 17–29. https://doi.org/10.1016/j.jas.2017.08.003

5. Barber, K., Langdon, P., Blundell, A., 2008. Dating the Glen Garry tephra: a widespread late-Holocene marker horizon in the peatlands of northern Britain. The Holocene 18, 31–43. https://doi.org/10.1177/0959683607085594

6. Beck, H., Zimmermann, N., McVicar, T. et al. 2018. Present and future Köppen-Geiger climate classification maps at 1-km resolution. Scientific Data 5, 180214. https://doi.org/10.1038/sdata.2018.214

7. Bennett, K.D., Boreham, S., Shárp, M.J., et al. 1992. Holocene history of environment, vegetation and human settlement on Catta Ness, Lunnasting, Shetland. Journal of Ecology 80, 241–273. https://doi.org/10.2307/2261010

8. Bigelow, G., Ferrante, S.M., Hall, S.T., et al. 2005. Researching catastrophic environmental changes on northern coastlines: A geoarchaeological case study from the Shetland Islands. Arctic Anthropology 42, 88–102. https://doi.org/10.1353/arc.2011.0043

9. Biguenet, M., Sabatier, P., Chaumillon, E., et al. 2021. A 1600 year-long sedimentary record of tsunamis and hurricanes in the Lesser Antilles (Scrub Island, Anguilla). Sedimentary Geology 412, 105806. https://doi.org/10.1016/j.sedgeo.2020.105806

10. Birnie, J.F., Gordon, J.E., Bennett, K.J., et al. (eds.) 1993. The Quaternary of Shetland: Field Guide. Quaternary Research Association, Cambridge.

11. Björck, S., Wohlfarth, B. (2001). ^{14}C chronostratigraphic techniques in paleolimnology. In: W.M. Last, W. M., Smol, J.P. (eds.), Tracking environmental change using lake sediments: Physical and chemical techniques, Kluwer Academic Publishers, Dordrecht, pp. 205-245.

12. Blaauw, M., Christen, J.A., 2011. Flexible paleoclimate age-depth models using an auto-regressive gamma process. Bayesian Analysis 6, 457–474. https://doi.org/10.1214/11-BA618

13. Blockley, S.P.E., Pyne-O'Donnell, S.D.F., Lowe, J.J., et al. 2005. A new and less destructive laboratory procedure for the physical separation of distal glass tephra shards from sediments. Quaternary Science Reviews 24, 1952–1960. https://doi.org/10.1016/j.quascirev.2004.12.008

14. Blott, S.J., Pye, K., 2001. Gradistat: A grain size distribution and statistics package for the analysis of unconsolidated sediments. Earth Surface Processes and Landforms 26, 1237–1248. https://doi.org/10.1002/esp.261

15. Bondevik, S., Mangerud, J., Dawson, S., et al. 2005. Evidence for three North Sea tsunamis at the Shetland Islands between 8000 and 1500 years ago. Quaternary Science Reviews 24, 1757–1775. https://doi.org/10.1016/j.quascirev.2004.10.018

16. Bradwell, T., Small, D., Fabel, D., et al. 2019. Pattern, style and timing of British–Irish Ice Sheet retreat: Shetland and northern North Sea sector. Journal of Quaternary Science 36, 681–722. https://doi.org/10.1002/jqs.3163

17. Brightspec, 2015. Technical Specifications bAxil Software Package. https://www.bright-spec.be/brightspec/?q=node/31 (accessed 8 December 2021).

18. Chagué, C., 2020. Applications of geochemical proxies in paleotsunami research. In: Engel, M., Pilarczyk, J., May, S.M. et al. (eds.), Geological records of tsunamis and other extreme waves.

Elsevier, Amsterdam, pp. 381-401. https://doi.org/10.1016/B978-0-12-815686-5.00018-3

19. Chaumillon, E., Bertin, X., Fortunato, A.B., et al. 2017. Storm-induced marine flooding: Lessons from a multidisciplinary approach. Earth-Science Reviews 165, 151–184. https://doi.org/10.1016/j.earscirev.2016.12.005

20. Clarke, M.L., Rendell, H.M., 2009. The impact of North Atlantic storminess on western European coasts: A review. Quaternary International 195, 31–41. https://doi.org/10.1016/j.quaint.2008.02.007

21. Costas, S., Jerez, S., Trigo, R.M., et al. 2012. Sand invasion along the Portuguese coast forced by westerly shifts during cold climate events. Quaternary Science Reviews 42, 15–28. https://doi.org/10.1016/j.quascirev.2012.03.008

22. Cuven, S., Paris, R., Falvard, S., et al. 2013. High-resolution analysis of a tsunami deposit: Case-study from the 1755 Lisbon tsunami in southwestern Spain. Marine Geology 337, 98–111. https://doi.org/10.1016/j.margeo.2013.02.002

23. Dargie, T., 1998. Sand dune vegetation survey of Scotland: Shetland. Volume 1: Main report. Scottish Natural Heritage Research, Survey and Monitoring Report No. 122.

24. Davies, S.M., Hoek, W.Z., Bohncke, J.P., et al. 2005. Detection of Lateglacial distal tephra layers in the Netherlands. Boreas 34, 123–135. https://doi.org/10.1111/j.1502-3885.2005.tb01010.x

25. Davies, S.J., Lamb, H.F., Roberts, S.J., 2015. Micro-XRF core scanning in palaeolimnology: Recent developments. In: Croudace, I.W., Rothwell, R.G. (eds.), Micro-XRF studies of sediment cores. Springer, Dordrecht, pp. 189–226. https://doi.org/10.1007/978-94-017-9849-5_7

26. Dawson, A.G., Dawson, S., Bondevik, S., 2006. A Late Holocene tsunami at Basta Voe, Yell, Shetland Isles. Scottish Geographical Journal 122, 100–108. https://doi.org/10.1080/00369220600917404

27. Dawson, A.G., Hickey, K., Holt, T., et al. 2002. Complex North Atlantic Oscillation (NAO) Index signal of historic North Atlantic storm-track changes. The Holocene 12, 363–369. https://doi.org/10.1191/0959683602hl552rr

28. Dawson, A.G., Hickey, K., Mayewski, P.A., et al. 2007. Greenland (GISP2) ice core and historical indicators of complex North Atlantic climate changes during the fourteenth century. The Holocene 17, 425–432. https://doi.org/10.1177/0959683607077010

29. Dawson, A., Elliott, L., Noone, S., et al. 2004 a. Historical storminess and climate 'see-saws' in the North Atlantic region. Marine Geology 210, 247–259. https://doi.org/10.1016/j.margeo.2004.05.011

30. Dawson, A.G., McIlveny, J., Warren, J., 2010. Winter gale day frequency in Shetland and Faeroes, AD 1866–1905: Links to sea ice history and the North Atlantic Oscillation. Scottish Geographical Journal 126, 141–152. https://doi.org/10.1080/14702541.2010.527857

31. Dawson, S., Smith, D.E., Jordan, J., et al. 2004 b. Late Holocene coastal sand movements in the Outer Hebrides, NW Scotland. Marine Geology 210, 281–306. https://doi.org/10.1016/j.margeo.2004.05.013

32. Dezileau, L., Sabatier, P., Blanchemanche, P., et al. 2011. Intense storm activity during the Little Ice Age on the French Mediterranean coast. Palaeogeography, Palaeoclimatology, Palaeoecology 299, 289–297. https://doi.org/10.1016/j.palaeo.2010.11.009

33. Dietze, E., Dietze, M., 2019. Grain-size distribution unmixing using the R package EMMAgeo. E&G Quaternary Science Journal 68, 29–46. https://doi.org/10.5194/egqsj-68-29-2019

34. Dietze, E., Hartmann, K., Diekmann, B., et al. 2012. An end-member algorithm for deciphering modern detrital processes from lake sediments of Lake Donggi Cona, NE Tibetan Plateau, China. Sedimentary Geology 243–244, 169–180. https://doi.org/10.1016/j.sedgeo.2011.09.014

35. Dry, F.T., Robertson, J.S., 1982. Orkney & Shetland: Soil and land capability for agriculture. Soil Survey of Scotland. The Macaulay Institute for Soil Research, Aberdeen.

36. Dugmore, A.J., Larsen, G., Newton, A.J., 1995. Seven tephra isochrones in Scotland. The Holocene 5, 257–266. https://doi.org/10.1177/095968369500500301

37. Elementar, 2020. Soli TOC® cube: TOC Analyzer. www.elementar.com/en/products/toc-analyzers/soli-toc-cube (accessed 8 December 2021).

38. Flinn, D., 1974. The coastline of Shetland. In: Goodier, R. (ed.), The natural environment of Shetland. Proceedings of the Nature Conservancy Council Symposium, Edinburgh, 29–30 January 1974. Nature Conservation Council, Edinburgh, pp. 13–23.

39. Folk, R.L., Ward, W.C., 1957. Brazos River bar [Texas]; A study in the significance of grain size parameters. Journal of Sedimentary Research 27, 3–26. https://doi.org/10.1306/74D70646-2B21-11D7-8648000102C1865D

40. Fritsch GmbH, 2020. Product leaflet laser particle measuring devices: Analysette 22 NeXT. https://www.fritsch-international.com/particle-sizing/overview/details/product/laser-particle-sizer-analysette-22-next-nano/downloads/ (accessed 1 June 2022).

41. Geotek, 2021. Geotek core logging systems. www.geotek.co.uk/products (accessed 8 December 2021).

42. Gilbertson, D.D., Schwenninger, J.-L., Kemp, R.A., et al. 1999. Sand-drift and soil formation along an exposed North Atlantic coastline: 14,000 years of diverse geomorphological, climatic and human impacts. Journal of Archaeological Science 26, 439–469. https://doi.org/10.1006/jasc.1998.0360

43. Gill, J.B., 1981. Orogenic andesites and plate tectonics. Springer, Berlin, Heidelberg, pp. 392. https://doi.org/10.1007/978-3-642-68012-0

44. Gillen, C., 2003. Geology and landscapes of Scotland. Terra, Harpenden.

45. Giraudeau, J., Grelaud, M., Solignac, S., et al. 2010. Millennial-scale variability in Atlantic water advection to the Nordic Seas derived from Holocene coccolith concentration records. Quaternary Science Reviews 29, 1276–1287. https://doi.org/10.1016/j.quascirev.2010.02.014

46. Goslar, T., Czernik, J., Goslar, E., 2004. Low-energy ^{14}C-AMS in Poznań Radiocarbon Laboratory, Poland. Nuclear Instruments and Methods in Physics Research Section B: Beam Interactions with Materials and Atoms 223–224, 5–11. https://doi.org/10.1016/j.nimb.2004.04.005

47. Goslin, J., Clemmensen, L.B., 2017. Proxy records of Holocene storm events in coastal barrier systems: Storm-wave induced markers. Quaternary Science Reviews 174, 80–119. https://doi.org/10.1016/j.quascirev.2017.08.026

48. Goslin, J., Fruergaard, M., Sander, L., et al. 2018. Holocene centennial to millennial shifts in North-Atlantic storminess and ocean dynamics. Scientific Reports 8, 12778. https://doi.org/10.1038/s41598-018-29949-8

49. Hall, A.M., Hansom, J.D., Williams, D.M., et al. 2006. Distribution, geomorphology and lithofacies of cliff-top storm deposits: Examples from the high-energy coasts of Scotland and Ireland. Marine Geology 232, 131–155. https://doi.org/10.1016/j.margeo.2006.06.008

50. Hall, V.A., Pilcher, J.R., 2002. Late-Quaternary Icelandic tephras in Ireland and Great Britain: detection, characterization and usefulness. The Holocene 12, 223–230. https://doi.org/10.1191%2F0959683602hl538rr

51. Hall, A.M., Hansom, J.D., Jarvis, J., 2008. Patterns and rates of erosion produced by high energy wave processes on hard rock headlands: The Grind of the Navir, Shetland, Scotland. Marine Geology 248, 28–46. https://doi.org/10.1016/j.margeo.2007.10.007

52. Hall, A.M., Hansom, J.D., Gordon, J.E., 2021. Shetland. In: Ballantyne, C.K., Gordon, J.E. (eds.), Landscapes and Landforms of Scotland. Springer, Cham, pp. 135–150. https://doi.org/10.1007/978-3-030-71246-4_7

53. Hansom, J.D., Hall, A.M., 2009. Magnitude and frequency of extra-tropical North Atlantic cyclones: A chronology from cliff-top storm deposits. Quaternary International 195, 42–52. https://doi.org/10.1016/j.quaint.2007.11.010

54. Hunt, J.B., Hill, P.G., 1996. An inter-laboratory comparison of the electron probe microanalysis of glass geochemistry. Quaternary International 34–36, 229-241. https://doi.org/10.1016/1040-6182(95)00088-7

55. Hurrell, J.W., 1995. Decadal trends in the North Atlantic Oscillation: regional temperature and precipitation. Nature 269, 676–679. DOI: 10.1126/science.269.5224.676

56. Irvine, S.G., 1968. An outline of the climate of Shetland. Weather 23, 392–403. https://doi.org/10.1002/j.1477-8696.1968.tb03013.x

57. Jarosewich, E., Nelen, J.A., Norberg, J.A., 1980. Reference samples for electron microprobe analysis. Geostandards Newsletter 4, 43–47. https://doi.org/10.1111/j.1751-908X.1980.tb00273.x

58. Kassambara, A., 2017. Practical guide to principal component methods in R (Multivariate Analysis Book 2). STHDA.

59. Kelley, J.T., Kelley, A.R., Sorrell, L., et al. 2018. Evidence for a former transgressive dune field: Shetland Islands, United Kingdom. Journal of Coastal Research 34, 1289–1302. https://doi.org/10.2112/JCOASTRES-D-17-00127.1

60. Kern, O.A., Koutsodendris, A., Mächtle, B., et al. 2019. XRF core scanning yields reliable semiquantitative data on the elemental composition of highly organic-rich sediments: Evidence from the Füramoos peat bog (Southern Germany). Science of the Total Environment 697, 134110. https://doi.org/10.1016/j.scitotenv.2019.134110

61. Kuehn, S.C., Froese, D.G., Shane, P.A.R., 2011. The INTAV intercomparison of electron-beam microanalysis of glass by tephrochronology laboratories: Results and recommendations. Quaternary

International 246, 19–47. https://doi.org/10.1016/j.quaint.2011.08.022

62. Kylander, M.E., Söderlindh, J., Schenk, F., et al. 2020. It's in your glass: A history of sea level and storminess from the Laphroaig bog, Islay (southwestern Scotland). Boreas 49, 152–167. https://doi.org/10.1111/bor.12409

63. Lamb, H.H., 1991. Historic storms of the North Sea, British Isles and Northwest Europe. Cambridge University Press, Cambridge.

64. Langdon, P.G., Barber, K.E., 2001. New Holocene tephras and a proxy climate record from a blanket mire in northern Skye, Scotland. Journal of Quaternary Science 16, 753–759. https://doi.org/10.1002/jqs.655

65. Larsen, G., Dugmore, A., Newton, A., 1999. Geochemistry of historical-age silicic tephras in Iceland. The Holocene 9, 463–471. https://doi.org/10.1191%2F095968399669624108

66. Larsen, G., Eiríksson, J., Gudmundsdóttir, E.R., 2014. Last millennium dispersal of air-fall tephra and ocean-rafted pumice towards the north Icelandic shelf and the Nordic seas. Geological Society, London, Special Publications 398, 113–140. https://doi.org/10.1144/SP398.4

67. Le Bas, M.J., Le Maitre, R.W., Streckeisen, A., et al. 1986. A chemical classification of volcanic rocks based on the total alkali-silica diagram. Journal of Petrology 27, 745–750. https://doi.org/10.1093/petrology/27.3.745

68. Liu K.-B., 2004. Palaeotempestology: principles, methods, and examples from Gulf Coast lake sediments. In: Murname R.J., Liu K.-B. (eds.) Hurricanes and typhoons: past, present and future. Columbia University Press, New York, pp. 13–57.

69. Liu, K., Fearn, M.L., 2000. Reconstruction of prehistoric landfall frequencies of catastrophic hurricanes in northwestern Florida from lake sediment records. Quaternary Research 54, 238–245. https://doi.org/10.1006/qres.2000.2166

70. May, S.M., Engel, M., Brill, D., et al. 2013. Coastal hazards from tropical cyclones and extratropical winter storms based on Holocene storm chronologies. In: Finkl, C. (ed.), Coastal Hazards. Springer, Dordrecht, pp. 557–585. https://doi.org/10.1007/978-94-007-5234-4_20

71. McIlvenny, J.D., Muller, F., Dawson, A., 2013. A 7600-year sedimentary record of climatic instability in Dunnet Bay, North Scotland. Marine Geology 335, 100–113. https://doi.org/10.1016/j.margeo.2012.10.014

72. Meeker, L.D., Mayewski, P.A., 2002. A 1400-year high-resolution record of atmospheric circulation over the North Atlantic and Asia. The Holocene 12, 257–266. https://doi.org/10.1191/0959683602hl542ft

73. Met Office, 2016. Northern Scotland: Climate. https://www.metoffice.gov.uk/binaries/content/assets/metofficegovuk/pdf/weather/learn-about/uk-past-events/regional-cli-mates/northern-scotland_-climate---met-office.pdf (accessed 8 December 2021).

74. Met Office, 2021. Historic station data – Lerwick. https://www.metoffice.gov.uk/pub/data/weather/uk/climate/stationdata/lerwickdata.txt (accessed 8 December 2021).

75. Morton, R.A., Gelfenbaum, G., Jaffe, B.E., 2007. Physical criteria for distinguishing sandy tsunami and storm deposits using modern examples. Sedimentary Geology 200, 184–207.

https://doi.org/10.1016/j.sedgeo.2007.01.003

76. Moskalewicz, D., Szczuciński, W., Mroczek, P., et al. 2020. Sedimentary record of historical extreme storm surges on the Gulf of Gdańsk coast, Baltic Sea. Marine Geology 420, 106084. https://doi.org/10.1016/j.margeo.2019.106084

77. Murray, J., Pullar, L., 1908. Bathymetrical survey of the fresh-water lochs of Scotland. Royal Geographical Society, London.

78. Mykura, W., Flinn, D., May, F., 1976. British Regional Geology: Orkney and Shetland. Natural Environment Research Council, Institute of Geological Sciences, Edinburgh.

79. Orme, L.C., Davies, S.J., Duller, G.A.T., 2015. Reconstructed centennial variability of Late Holocene storminess from Cors Fochno, Wales, UK. Journal of Quaternary Science 30, 478–488. https://doi.org/10.1002/jqs.2792

80. Orme, L.C., Reinhardt, L., Jones, R.T., et al. 2016. Aeolian sediment reconstructions from the Scottish Outer Hebrides: Late Holocene storminess and the role of the North Atlantic Oscillation. Quaternary Science Reviews 132, 15–25. https://doi.org/10.1016/j.quascirev.2015.10.045

81. Osleger, D.A., Heyvaert, A.C., Stoner, J.S., et al. 2009. Lacustrine turbidites as indicators of Holocene storminess and climate: Lake Tahoe, California and Nevada. Journal of Paleolimnology 42, 103–122. https://doi.org/10.1007/s10933-008-9265-8

82. Petersen, M., Rohde, H., 1991. Sturmflut: Die großen Fluten an den Küsten Schleswig-Holsteins und in der Elbe, 3rd ed. Wachholtz, Neumünster, 182 pp.

83. Pilcher, J.R., Hall, V.A., McCormac, F.G., 1995. Dates of Holocene Icelandic volcanic eruptions from tephra layers in Irish peats. The Holocene 5, 103–110. https://doi.org/10.1177/095968369500500111

84. Pilcher, J., Bradley, R.S., Francus, P., et al. 2005. A Holocene tephra record from the Lofoten Islands, Arctic Norway. Boreas 34, 136–156. https://doi.org/10.1111/j.1502-3885.2005.tb01011.x

85. Plunkett, G., Pilcher, J.R., 2018. Defining the potential source region of volcanic ash in northwest Europe during the Mid- to Late Holocene. Earth-Science Reviews 179, 20–37. https://doi.org/10.1016/j.earscirev.2018.02.006

86. Plunkett, G.M., Pilcher, J.R., McCormac, F.G., et al. 2004. New dates for first millennium BC tephra isochrones in Ireland. The Holocene 14, 780–786. https://doi.org/10.1191/0959683604hl757rr

87. Pouzet, P., Maanan, M., 2020. Climatological influences on major storm events during the last millennium along the Atlantic coast of France. Scientific Reports 10, 12059. https://doi.org/10.1038/s41598-020-69069-w

88. Pringle, I.R., 1970. The structural geology of the North Roe area of Shetland. Geological Journal 7, 147–170. https://doi.org/10.1002/gj.3350070109

89. Rahmstorf, S., 2017. Rising hazard of storm-surge flooding. Proceedings of the National Academy of Sciences 114, 11806–11808. https://doi.org/10.1073/pnas.1715895114

90. Reimer, P.J., Austin, W.E.N., Bard, E., et al. 2020. The IntCal20 Northern Hemisphere radiocarbon age calibration curve (0–55 cal kBP). Radiocarbon 62, 725–757. https://doi.org/10.1017/RDC.2020.41

91. Sabatier, P., Dezileau, L., Condomines, M., et al., 2008. Reconstruction of paleostorm events in a coastal lagoon (Hérault, South of France). Marine Geology 251, 224–232. https://doi.org/10.1016/j.margeo.2008.03.001

92. Sabatier, P., Dezileau, L., Colin, C., et al. 2012. 7000 years of paleostorm activity in the NW Mediterranean Sea in response to Holocene climate events. Quaternary Research 77, 1–11. https://doi.org/10.1016/j.yqres.2011.09.002

93. Schillereff, D.N., Chiverrell, R.C., Macdonald, N., et al. 2014. Flood stratigraphies in lake sediments: A review. Earth-Science Reviews 135, 17–37. https://doi.org/10.1016/j.earscirev.2014.03.011

94. Schindelin, J., Arganda-Carreras, I., Frise, E. et al. 2012. Fiji: an open-source platform for biological-image analysis. Nature Methods 9, 676–682. https://doi.org/10.1038/nmeth.2019

95. Seneviratne, S.I., Zhang, X., Adnan, M., et al. 2021. Weather and climate extreme events in a changing climate. In: Masson-Delmotte, V., Zhai, P., Pirani, A. et al. (eds.), Climate Change 2021: The Physical Science Basis. Contribution of Working Group I to the Sixth Assessment Report of the Intergovernmental Panel on Climate Change. Cambridge University Press, Cambridge and New York, pp. 1513–1766. https://doi.org/10.1017/9781009157896.013

96. Smith, J.T., Belova, N.V., Bulgakov, A.A., et al. 2005. The "Aquascope" simplified model for predicting ^{89,90}Sr, ^{131}I and ^{134,137}Cs in surface waters after a large-scale radioactive fallout. Health Physics 89, 628–644. https://doi.org/10.1097/01.hp.0000176797.66673.b7

97. Soil Survey of Scotland, 1982. Orkney and Shetland. The Macaulay Institute for Soil Research, Aberdeen.

98. Sommerville, A.A., Hansom, J.D., Sanderson, D., et al. 2003. Optically stimulated luminescence dating of large storm events in Northern Scotland. Quaternary Science Reviews 22, 1085–1092. https://doi.org/10.1016/S0277-3791(03)00057-X

99. Stewart, H., Bradwell, T., Bullard, J., et al. 2017. 8000 years of North Atlantic storminess reconstructed from a Scottish peat record: implications for Holocene atmospheric circulation patterns in Western Europe. Journal of Quaternary Science 32, 1075–1084. https://doi.org/10.1002/jqs.2983

100. Swindles, G.T., Galloway, J., Outram, Z., et al. 2013. Re-deposited cryptotephra layers in Holocene peats linked to anthropogenic activity. The Holocene 23, 1493–1501. https://doi.org/10.1177/0959683613489586

101. Swindles, G.T., Galloway, J.M., Macumber, A.L., et al. 2018. Sedimentary records of coastal storm surges: Evidence of the 1953 North Sea event. Marine Geology 403, 262–270. https://doi.org/10.1016/j.margeo.2018.06.013

102. Thorarinsson, S., 1981. Greetings from Iceland. Ash-falls and volcanic aerosols in Scandinavia. Geografiska Annaler: Series A, Physical Geography 63, 109–118. https://doi.org/10.1080/04353676.1981.11880024

103. Tisdall, E.W., McCulloch, R.D., Sanderson, D., et al. 2013. Living with sand: A record of landscape change and storminess during the Bronze and Iron Ages Orkney, Scotland. Quaternary International 308–309, 205–215. https://doi.org/10.1016/j.quaint.2013.05.016

104. Trouet, V., Esper, J., Graham, N.E., et al. 2009. Persistent positive North Atlantic oscillation mode dominated the Medieval Climate Anomaly. Science 324, 78–80. https://doi.org/10.1126/science.1166349

105. Trouet, V., Scourse, J.D., Raible, C.C., 2012. North Atlantic storminess and Atlantic Meridional Overturning Circulation during the last Millennium: Reconciling contradictory proxy records of NAO variability. Global and Planetary Change 84–85, 48–55. https://doi.org/10.1016/j.gloplacha.2011.10.003

106. Turney, C.S.M., 1998. Extraction of rhyolitic component of Vedde microtephra from minerogenic lake sediments. Journal of Paleolimnology 19, 199–206. https://doi.org/10.1023/A:1007926322026

107. UK Centre for Ecology & Hydrology, 2004. UK Lakes Portal – Loch of Flugarth. https://eip.ceh.ac.uk/apps/lakes/detail.html#wbid=274 (accessed 8 December 2021).

108. Vakhrameeva, P, Portnyagin, M., Ponomareva, V., et al. 2020. Identification of Icelandic tephras from the last two millennia in the White Sea region (Vodoprovodnoe peat bog, northwestern Russia). Journal of Quaternary Science 35, 493–504. https://doi.org/10.1002/jqs.3190

109. Wahl, T., Haigh, I.D., Woodworth, P.L., et al. 2013. Observed mean sea level changes around the North Sea coastline from 1800 to present. Earth-Science Reviews, 124, 51–67. https://doi.org/10.1016/j.earscirev.2013.05.003

110. Wastegård, S., Rundgren, M., Schoning, K., et al. 2008. Age, geochemistry and distribution of the mid-Holocene Hekla-S/Kebister tephra. The Holocene 18, 539–549. https://doi.org/10.1177/0959683608089208

111. Watson, E.J., Swindles, G.T., Lawson, I.T., et al. 2016. Do peatlands or lakes provide the most comprehensive distal tephra records? Quaternary Science Reviews 139, 110–128. https://doi.org/10.1016/j.quascirev.2016.03.011

112. Wheeler, D., Garcia-Herrera, R., Wilkinson, C.W., et al. 2010. Atmospheric circulation and storminess derived from Royal Navy logbooks: 1685 to 1750. Climatic Change 101, 257–280. https://doi.org/10.1007/s10584-009-9732-x

113. Wilson, P., McGourty, J., Batema, M.D., 2004. Mid-to late-Holocene coastal dune event stratigraphy for the north coast of Northern Ireland. The Holocene 14, 406–416. https://doi.org/10.1191/0959683604hl716rp

114. Wöffler, T.E., 2016. Optimierung des Küsten- und Hochwasserschutzes auf den Halligen. PhD Dissertation, RWTH Aachen University, 245 pp. https://doi.org/10.18154/RWTH-2017-04570
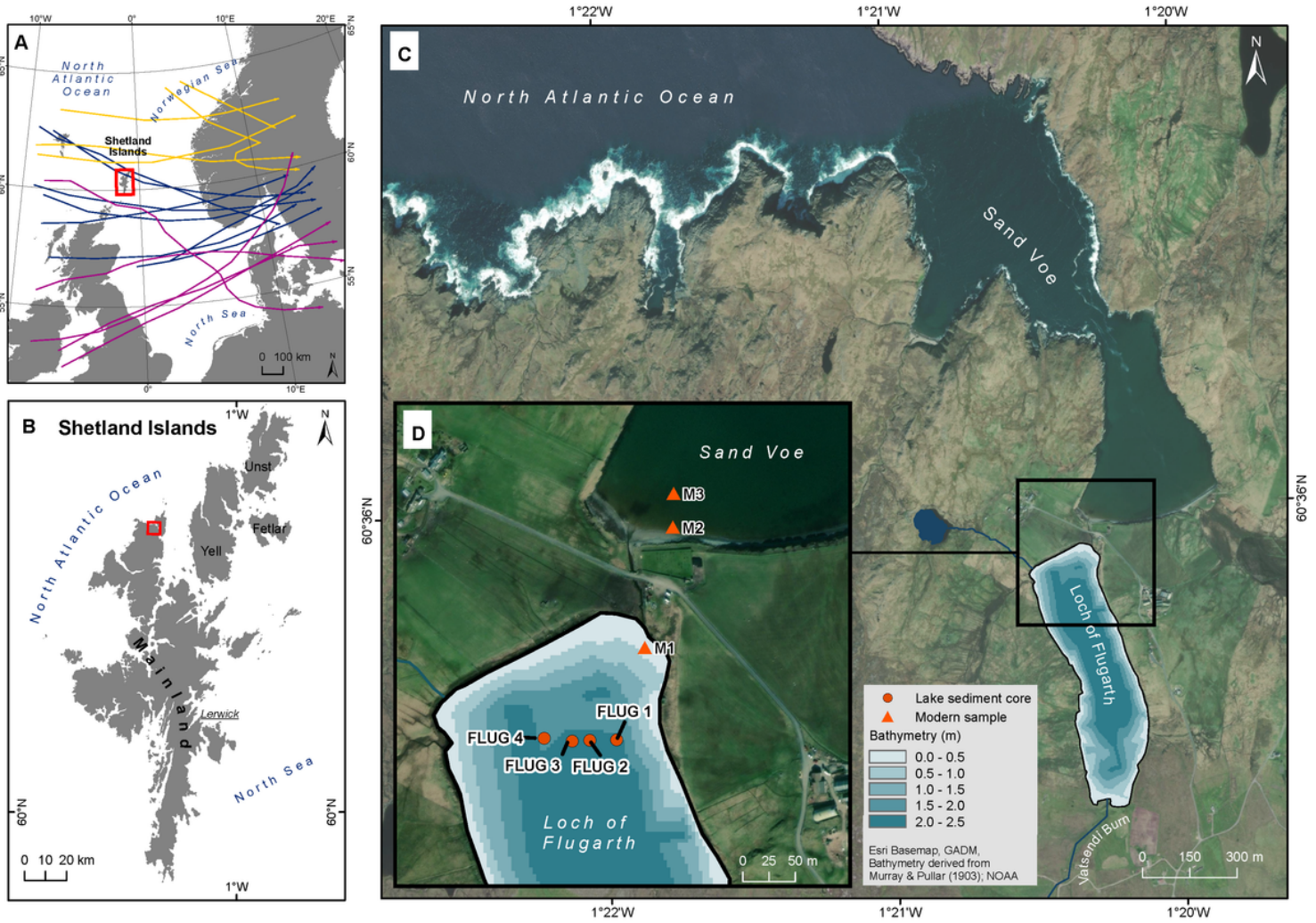
Figures

Figure 1

Map of the study area. **(a)** Three different storm track types cause storm surges at the North Sea Coast: The Scandinavian type (yellow), the Skagerrak type (blue), and the Jutland type (pink) (from Wöffler, 2016, modified after Petersen and Rohde, 1991). **(b)** The Shetland Islands with the study area in northwestern Mainland. **(c)** Sand Voe bay. **(d)** Location of Loch Flugarth and position of the lake sediment drilling cores (FLUG 1 – 4), and the modern environmental samples M1 - M3.
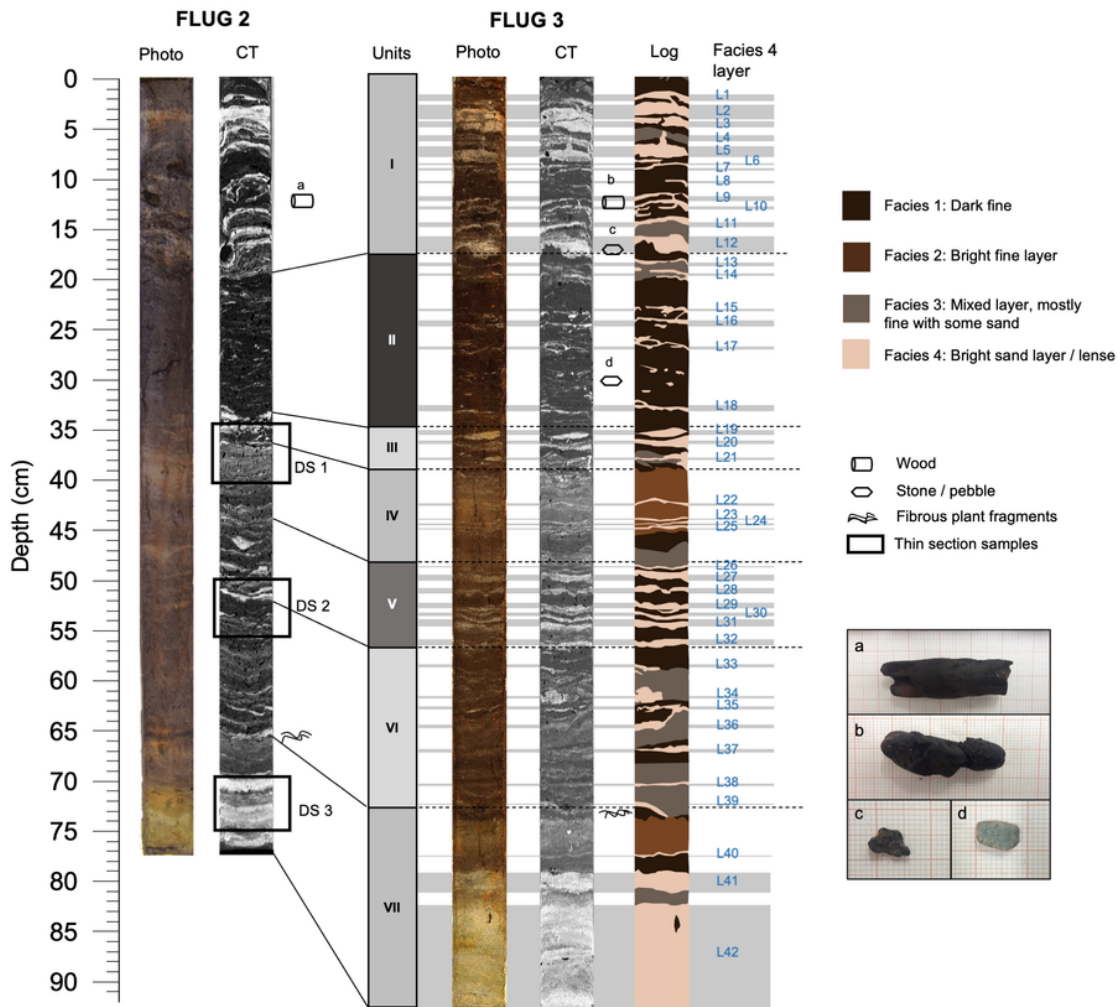
Figure 2

Overview of the lithostratigraphy. Left: Photograph and CT scan of FLUG 2. Middle: Evaluated lithostratigraphical sections of FLUG 3, photograph, CT scan and schematic lithostratigraphy of FLUG 3; Facies 4 layer, number in blue. Right below: Photographs of wood (a + b) and stones (c + d) found during sampling.
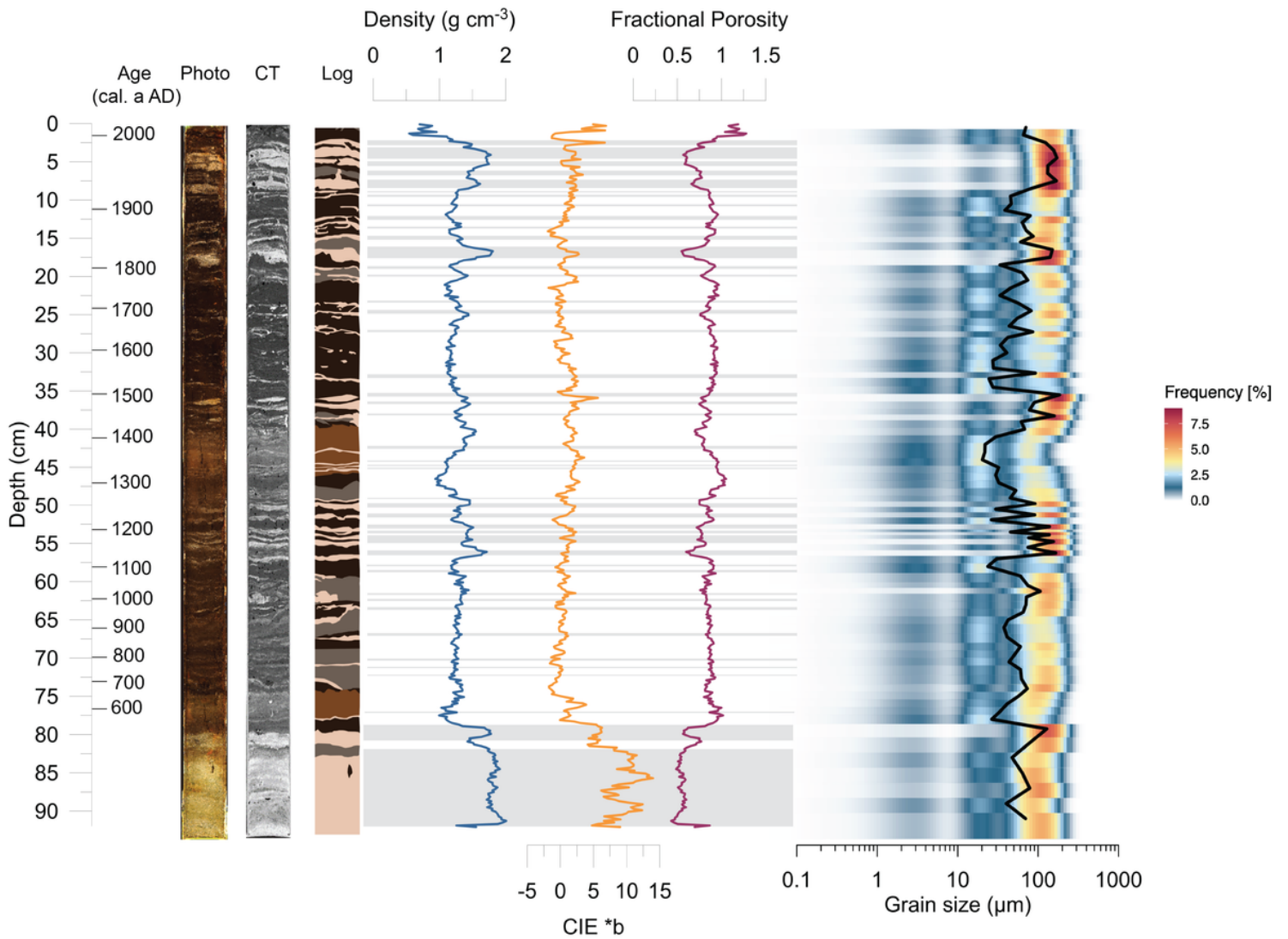
Figure 3

Sedimentological results of FLUG 3. From left to right: Photography, CT scan, lithostratigraphy (Log), density (blue line), CIE colour *b covering the blue-yellow axis colour spectra (yellow line), fractional porosity (red line), and a heatmap showing the grain size distribution frequency and the mean grain size (black line).
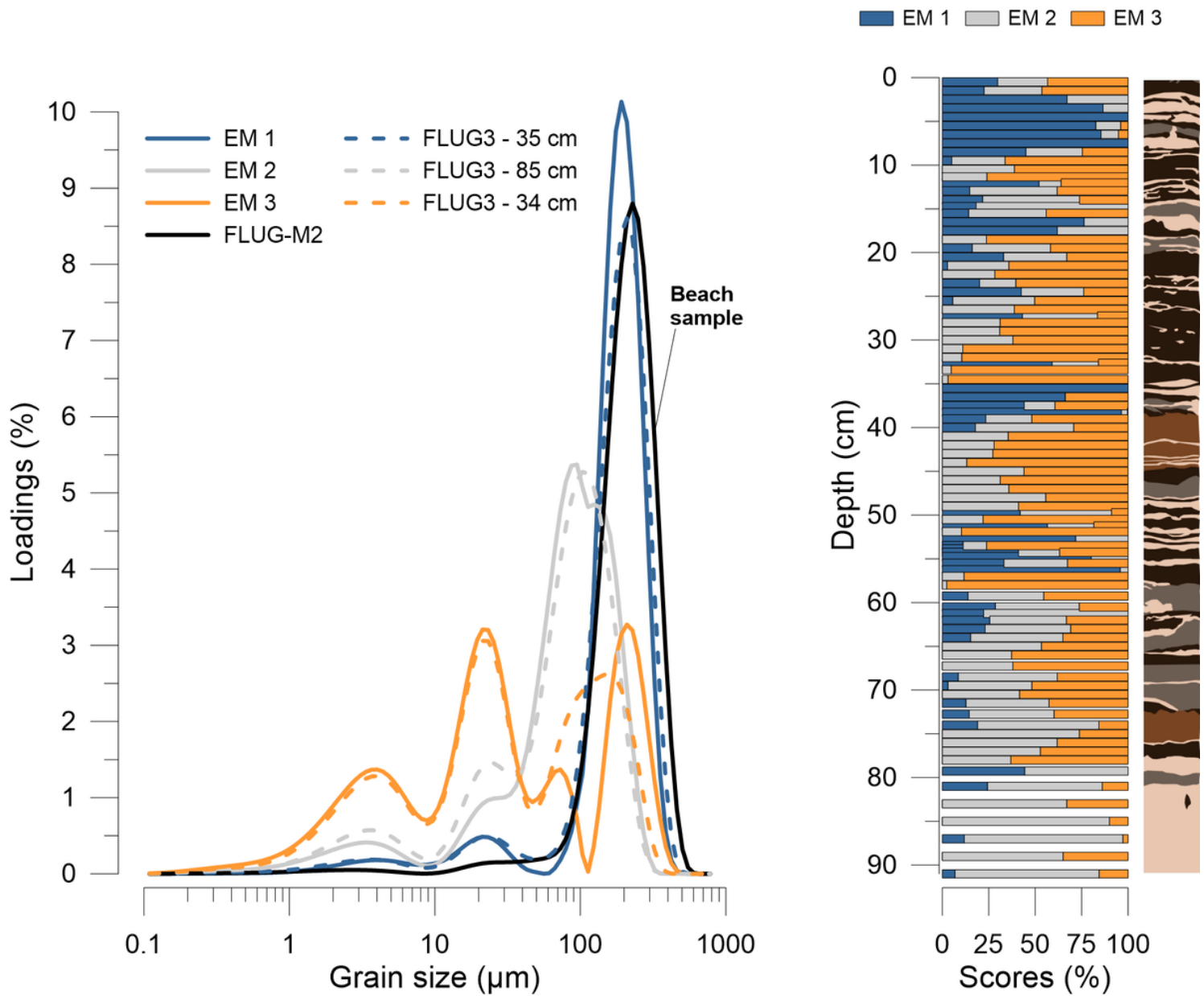
Figure 4

End-member modelling analysis showing: **(a)** the loadings of grain size distribution frequency with the three different end-member together with corresponding samples and **(b)** the scores for each end-member in percent.
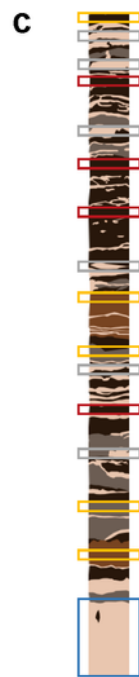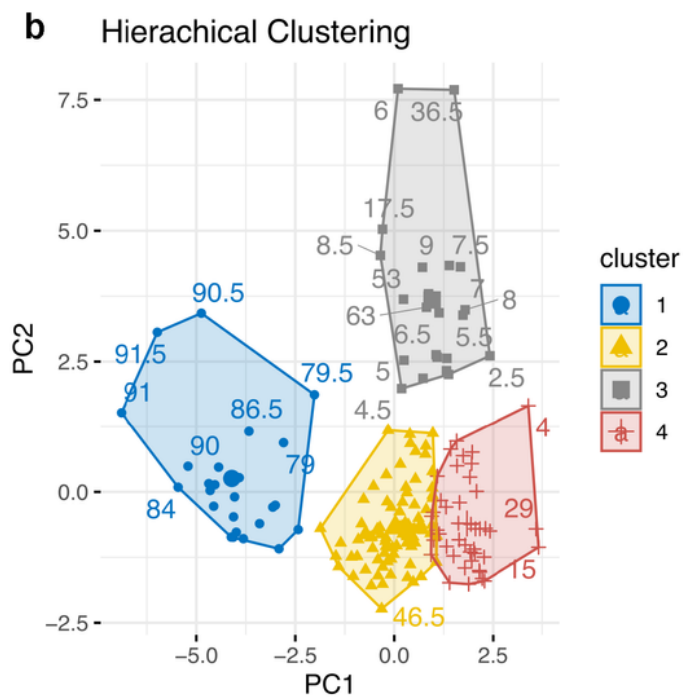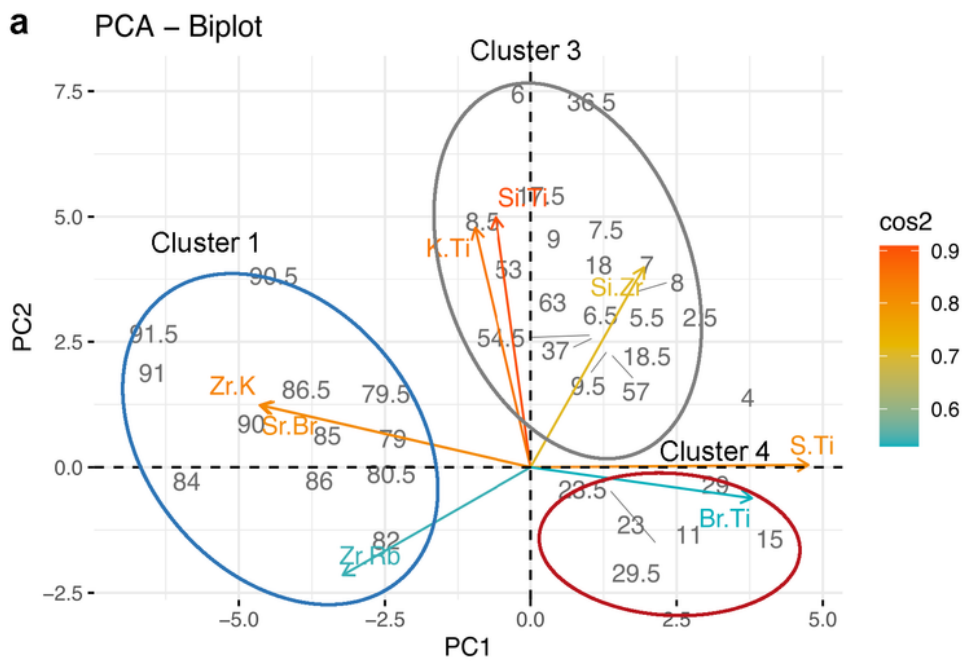
Figure 5

Biplots showing the results of the principal component analysis (PCA) and hierarchical clustering of principal components (HCPC). **(a)** Numbers indicate the depths (individuals) in cm b.s.. The variables (element ratios) of the PCA are represented by arrows. The length of the arrows indicates the degree of representativeness of each variable in relation to the first two dimensions. The variable cos2 illustrates the quality of representation of the variables on the factor map. The circles show the three different

groups of samples that were separated by the PCA matching the clusters of the HCPC **(b)** Factor map of the HCPC with four different clusters. Numbers indicate the depths (individuals) in cm b.s. **(c)**Core FLUG 3 with provenance of samples shown in the PCA biplot and the HCPC. Colours of the frames refer to colours of the grouping in the HCPC plot.
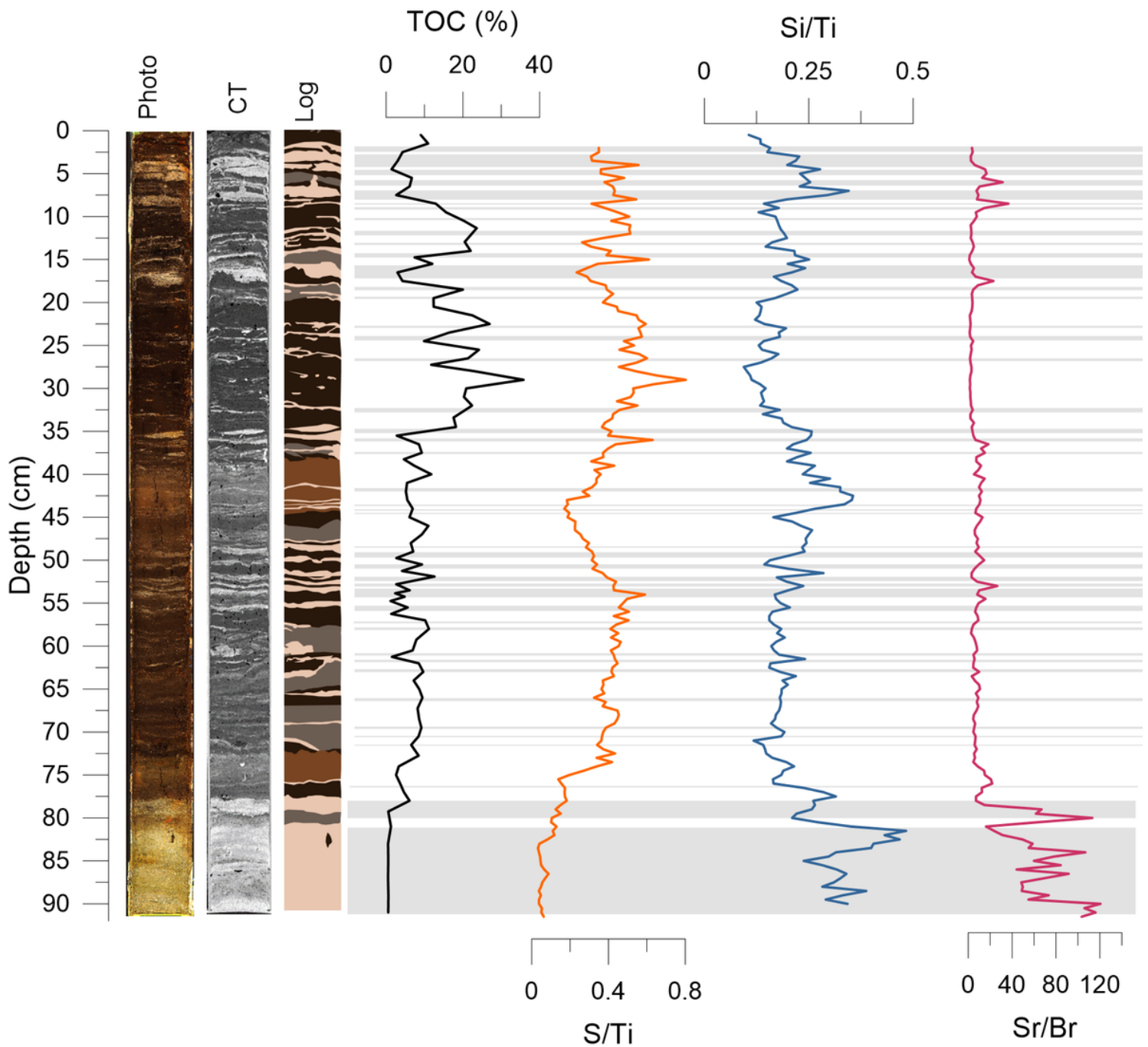

Figure 6

Geochemical proxies of FLUG 3. From left to right: Photograph, CT scan, lithostratigraphy, total organic carbon (TOC) (black), S/Ti (orange), Si/Ti (blue), and Sr/Br (pink).
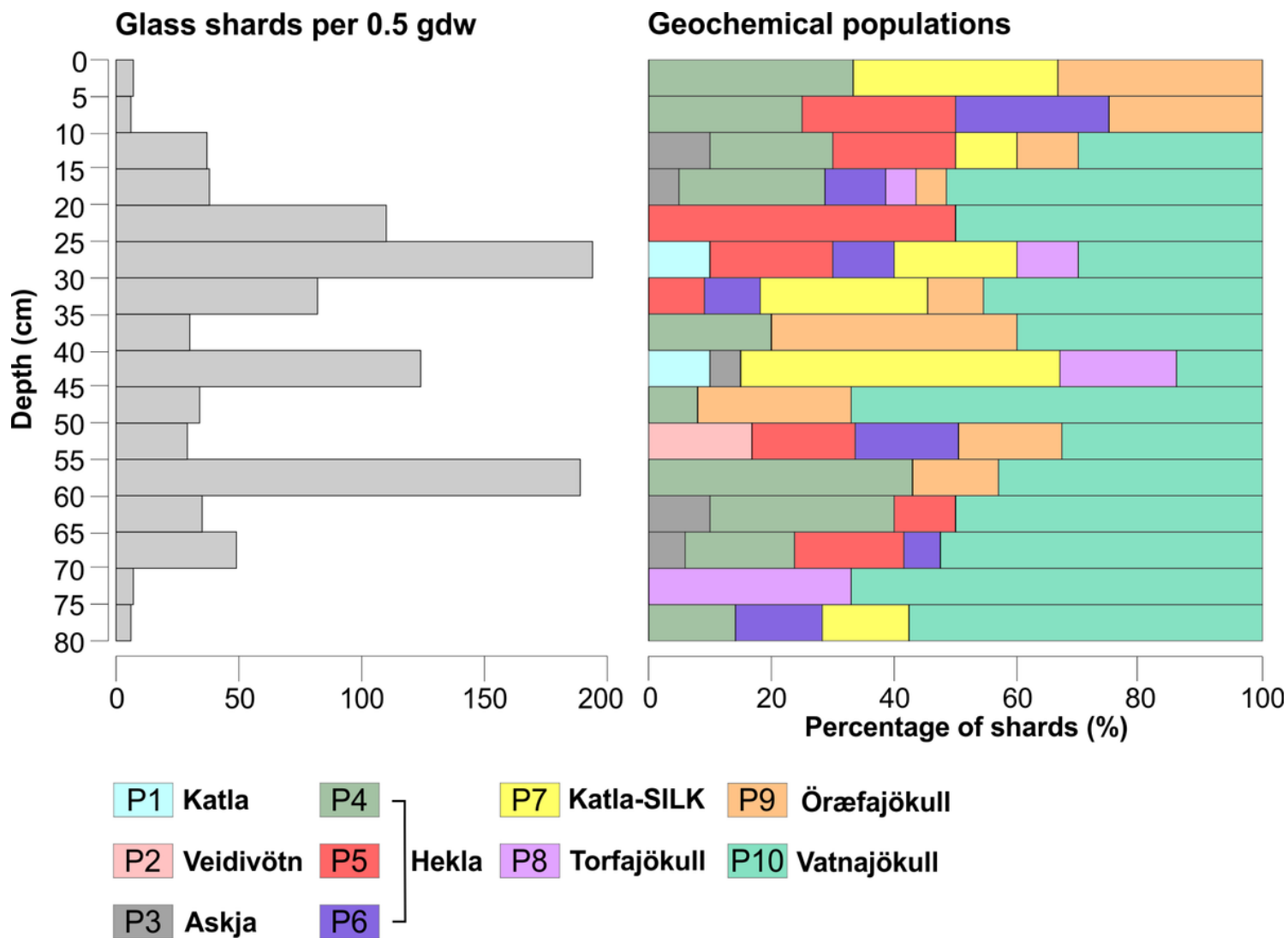
Figure 7

Cryptotephra record of core FLUG 3 including shard counts and glass geochemical populations in the 2.3–2.5 g cm^{-3} density fraction. Figure legend indicates volcanic sources of the glass populations as inferred in this study.
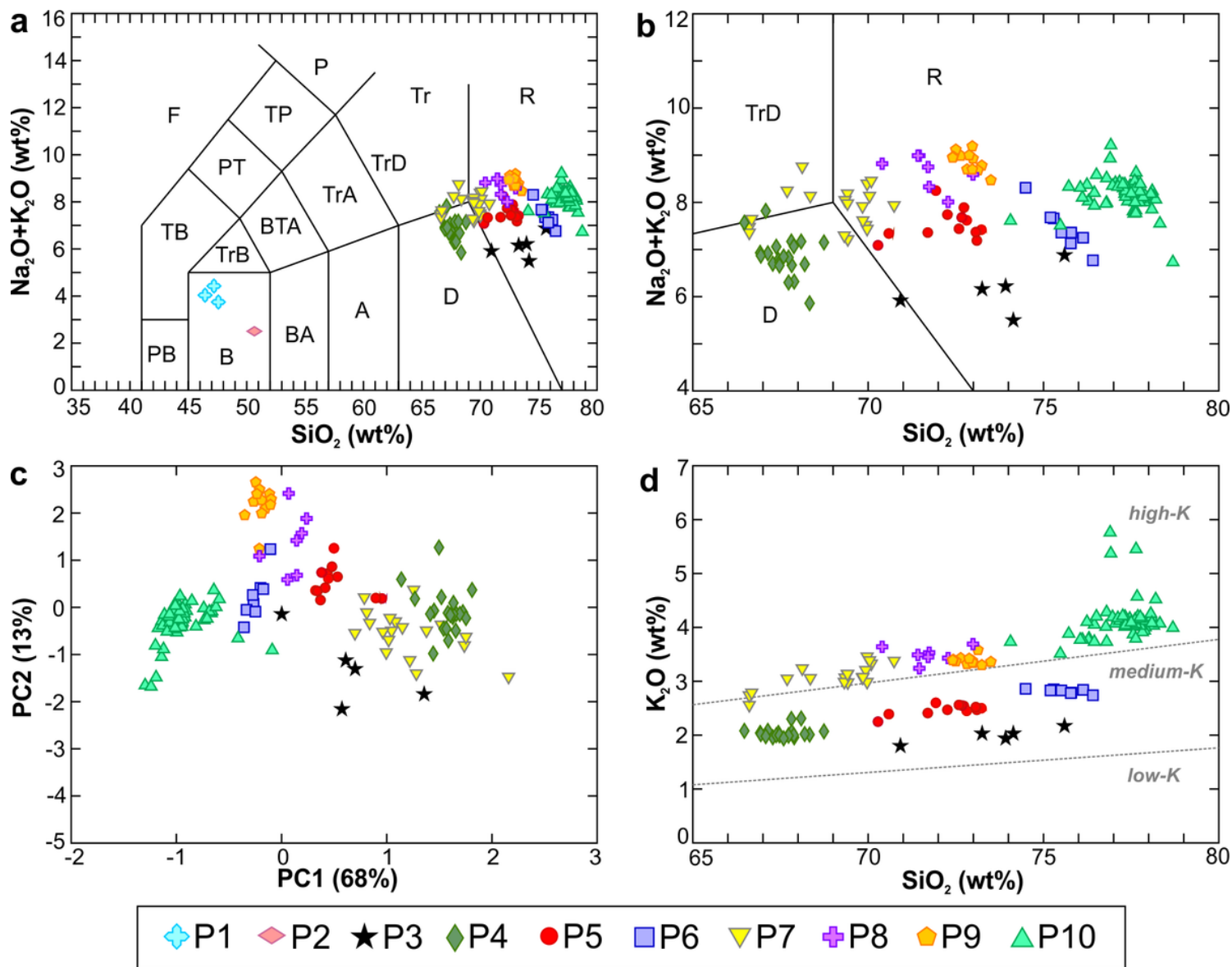
Figure 8

Glass geochemical populations within the FLUG 3 cryptotephra record. **(a)** Total alkali *vs.* silica classification diagram (Le Bas et al., 1986) showing all geochemical populations and **(b)** a close-up showing only silicic glass populations. **(c)** Results of principal component analysis of major-element data as a plot of first and second principal components (PC) comparing silicic glass populations. **(d)** K_2O *vs.* SiO_2 plot for silicic glass populations. Low-, medium- and high-K fields are shown after Gill (1981). Rock types: A − andesite; B − basalt; BA − basaltic andesite; BTA − basaltic trachyandesite; D − dacite; F − foidite; P − phonolite; PB − picrobasalt; PT − phonotephrite; R − rhyolite; TB − tephrite or basanite; TP − tephriphonolite; Tr − trachyte; TrA − trachyandesite; TrB − trachybasalt; TrD − trachydacite.
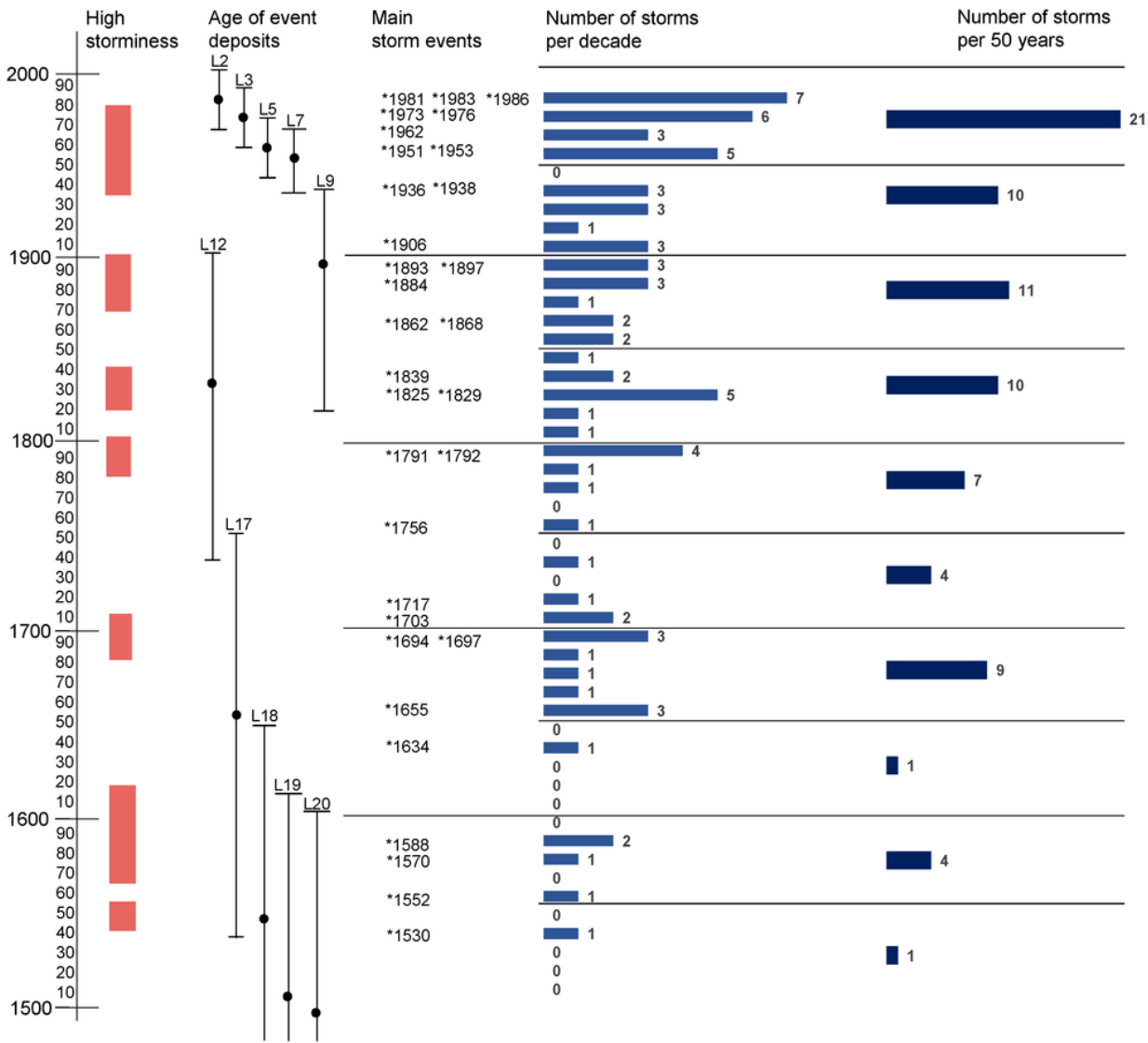
Figure 9

Overview of the periods with high storm frequency (red bars), age of event deposits (black points indicate the mean age), the main storm events, and the number of storms per decade, and half-century after Lamb (1991) between 1500 and 1989.
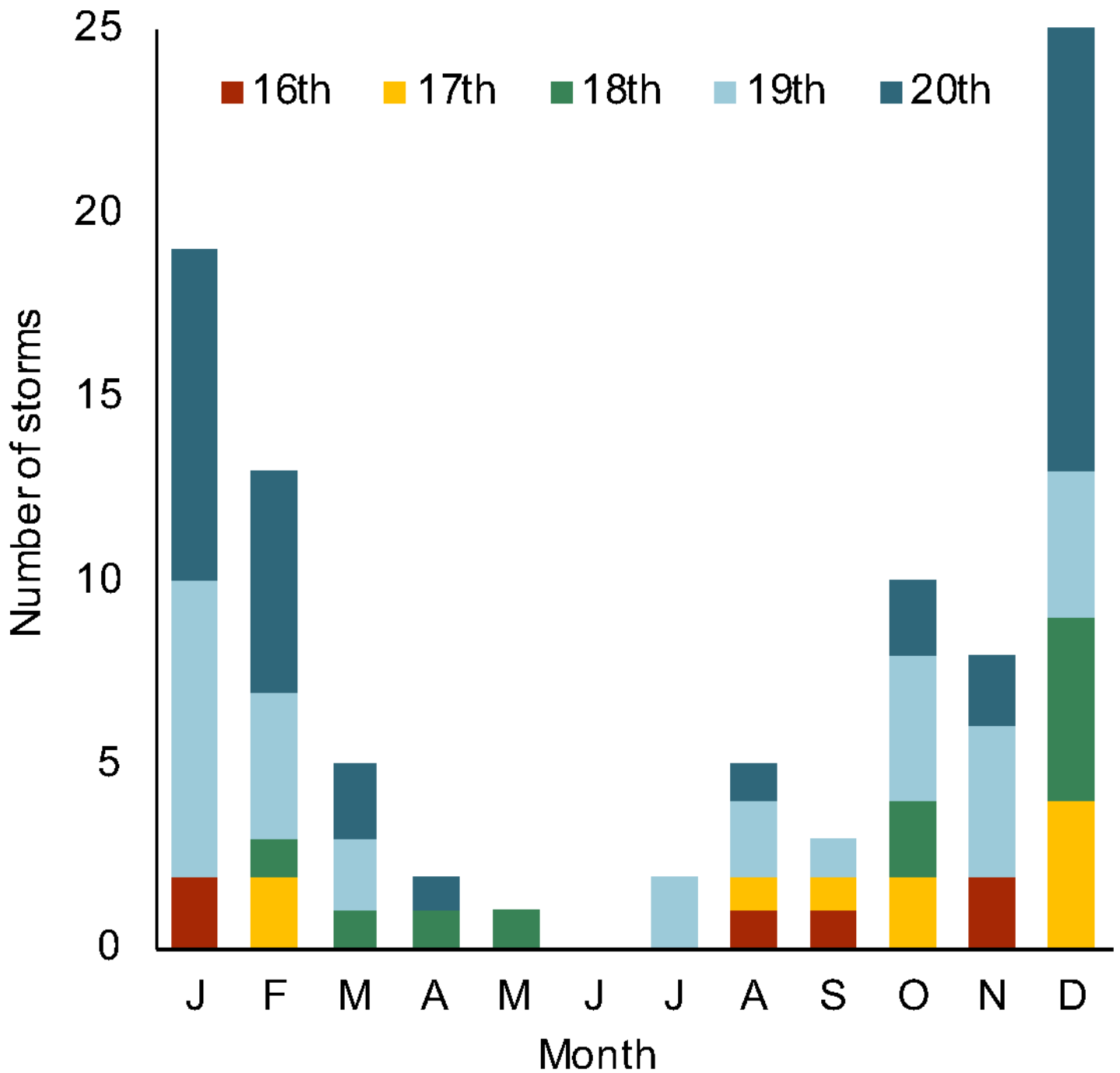
Figure 10

Column chart showing storms per month for each century from 1500 to 2000 to indicate changes in seasonality of storms (after Lamb, 1991). Storm descriptions missing information about the month of the storm were not included, which resulted in data gaps especially in the 16th and 17th centuries.
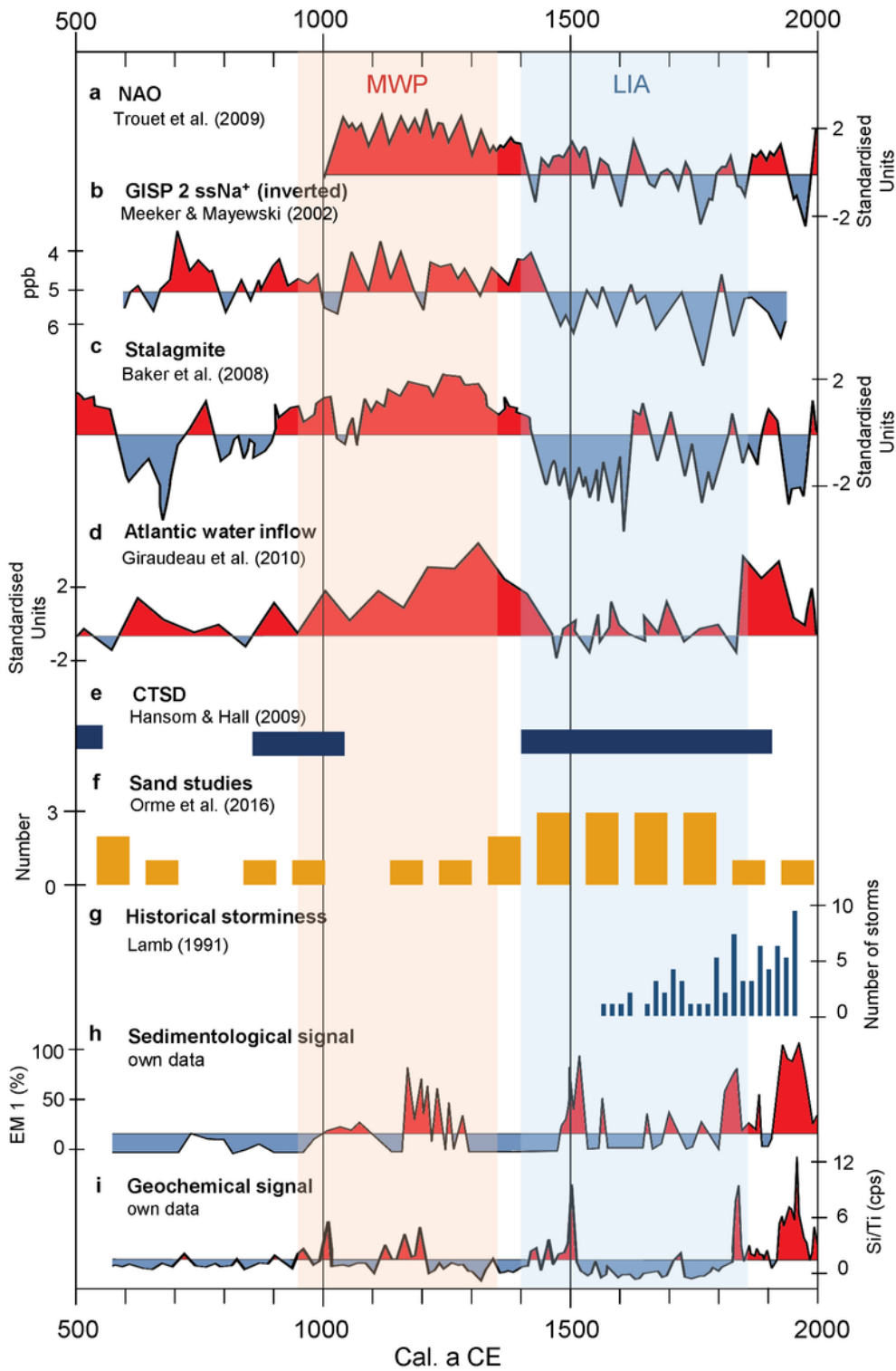
Figure 11

Comparison between NAO, different storminess studies and the data of the current study over the last 1500 years (modified after Orme et al., 2016). Larger climate anomalies such as the MWP and the LIA are presented in red and blue, respectively. **(a)** Winter (DJF) NAO reconstruction (Trouet et al., 2009). **(b)** Smoothed Greenland's sea salt influences (ssNa+) of core GISP2 (Meeker and Mayewski, 2002). **(c)** Stalagmite proxy from a Scottish cave (Baker et al., 2015). **(d)** Reconstruction of Atlantic water inflow in

the Norwegian Sea derived by concentrations of coccolith *Gephyrocapsa muellerae* (Giraudeau et al., 2010). **(e)** Cliff-top storm deposits on the Shetland Islands (Hansom and Hall, 2009). **(f)** Number of studies reporting sand transport in Scotland and Northern Ireland in the respective year (Orme et al., 2016). **(g)** Number of storms per 20 years from historical documents for northern Scotland and northern North Sea (Lamb, 1991). **(h)** Current study: Sedimentological signal of storminess by EM1. **(i)** Current study: Geochemical signal represented by XRF Si/Ti ratio. For **(h)** and **(i)**: Red peaks signify higher storminess.

Supplementary Files

This is a list of supplementary files associated with this preprint. Click to download.

- HessetalSupplement1.pdf
- Supplement2.xlsx